Toughness or strength? Regularization in phase-field fracture explained by the coupled criterion

Gergely Molnár, Aurélien Doitrand, Rafaël Estevez, Anthony Gravouil

Toughness or strength?
Regularization in phase-field fracture explained by the coupled criterion

Gergely Molnár[a,*], Aurélien Doitrand[b], Rafaël Estevez[c], Anthony Gravouil[a]

[a] *Univ Lyon, INSA-Lyon, CNRS UMR5259, LaMCoS, F-69621, France*
[b] *Univ Lyon, INSA-Lyon, CNRS UMR5510, MATEIS, F-69621, France*
[c] *Univ Grenoble Alpes, Grenoble INP, CNRS UMR5266, SIMaP, F-38000, France*

Abstract

In recent years the phase-field method and the coupled energy and stress-based criterion have attracted much attention due to their adaptability in modeling fractures. Both approaches have been successfully used to determine crack initiation and have compared well with real-life experiments. The phase-field method diffuses the crack surface into the volume of the solid, thus making the solution viable through variational techniques. The diffusion is controlled by an internal length scale, which is primarily considered to be a numerical aid without any real physical meaning. In this paper, we question the consideration that the internal length is only a numerical parameter, and assess its mechanical significance with the help of the coupled criterion. Through elaborate benchmark examples, the correlation between the two methods is demonstrated based on the critical loading, the crack topology, and the crack arrest length. We reveal that independently of the chosen aspect, the phase-field approach and the coupled criterion present excellent correspondence. We show that the correlation between tensile strength and length scale is unique for the standard phase-field formulation. Interestingly, we find that both stress and energy criteria are satisfied in the phase-field fracture, and this is explained by demonstrating the alteration in global energy release rate due to the regularization introduced by the smeared model.

Keywords: Coupled criterion, Phase-field, Internal length scale, Tensile strength, Crack arrest, Shear fracture, Energy release rate

1. Introduction

Fracture is one of the most feared failure modes in engineering as it manifests almost immediately and has devastating consequences. Cracks can appear at several spatial and temporal scales and in a variety of materials. The principals are similar in electronic, mechanical, or structural engineering problems as well as in seismology or biomechanics. Therefore, fracture is a common issue. However, a universal approach is still missing.

Phase-field fracture models have become more and more popular in recent years due to their adaptability and ease of use. These models can initiate, propagate, arrest, or even branch cracks with a unique formulation without any particular criterion. The principal idea for all diffuse models is that they approximate the discontinuity by a smeared damage field. In most of the models, a single length scale (l_c) is introduced, which controls the magnitude of the damage penetration into the solid. When l_c is reduced to 0, the original Griffith theory is recovered. Therefore, in most of the literature, the length scale parameter is considered a sacrifice, distorting the mechanical behavior but making fracture problems accessible to variational approaches.

The first theory to describe fracture propagation was proposed by Griffith (1924, 1921). He assumed that an already existing crack could grow if the released potential energy was sufficient to create the necessary fracture surfaces. According to this description, the toughness of the material can be described by a critical surface energy. This early work is based on the description of the elastic stress field around the crack tip that assumes traction free boundaries along the crack surfaces, resulting in a stress singularity at the crack tip. In reality, no material can support a singular stress field. Therefore, the concept of the process zone (PZ) was introduced in the late 1950s. This regularization alters both the stress field and the global energy release upon crack propagation. Various numerical methods take the fracture process zone into account in different ways.

*Corresponding author
Email address: gergely.molnar@insa-lyon.fr (Gergely Molnár)

Smeared approaches, such as the thick level set (TLS) (Moës et al., 2011) or the gradient damage models (Bourdin et al., 2000a; Miehe et al., 2010a) propose a potential alternative. Damage models use an internal length scale to diffuse the crack into the volume of the solid. In the TLS, the fracture topology is calculated based on geometrical considerations, while in the phase-field approach, an additional gradient flow equation is solved.

Both methods are based on the original Griffith (1924, 1921) solution. This stationary approach was updated by Francfort and Marigo (1998), who reformulated the local energy criterion to a global minimization problem. Though the idea was simple, this was the first step towards a variational formulation of fracture problems. Nevertheless, a conundrum persisted because the fracture was described using a surface domain in the volume. The solution was finally proposed by Bourdin et al. (2000a) motivated by the Mumford and Shah (1989) functional, which is the limit case of the Ambrosio and Tortorelli (1990) elliptic regularization function. Essentially, the crack density function was introduced by Miehe et al. (2010a) with an internal length scale (l_c), describing the transition towards the limiting case represented by a Griffith-like fracture. Since its introduction, the method has gained incredible popularity. Many modifications have been proposed to represent plasticity (Ambati et al., 2015; Fang et al., 2019), dynamic effects (Borden et al., 2012), fatigue (Lo et al., 2019; Mesgarnejad et al., 2019), interfacial damages (Nguyen et al., 2019), hydrogen assisted cracking (Martínez-Pañeda et al., 2018) or even hydraulic fractures (Wilson and Landis, 2016; Xia et al., 2017; Zhou et al., 2020).

Initially, l_c was introduced to facilitate the solution using numerical methods and to prevent any mesh dependence of the crack path. Pham and Marigo (2010a,b) theorized that this parameter should be identified separately as it represents the material's internal length (Freddi and Royer-Carfagni, 2010; Pham et al., 2011; Piero, 2013). Recently several works calibrated l_c to capture the maximum loading at failure to experiment (Kumar et al., 2020; Nguyen et al., 2016a; Tanné et al., 2018). Nguyen et al. (2016c,b) even identified the extent of the micro-damaged region around a discrete crack using micro-computed tomography. First Zhang et al. (2017), then Tanné et al. (2018) and most recently Kumar et al. (2020); Kumar and Lopez-Pamies (2020b) demonstrated that the variational formulation can establish the connection between stress and toughness based criteria. Phase-field methods can regularize the infinite critical load at infinitesimal crack lengths defined by the Griffith criterion. Reproducing a size effect observed a long time ago in experiments (Bažant, 1997; Chudnovsky, 2014; Issa et al., 2000). These groundbreaking papers successfully confirmed that l_c is necessary to calculate the critical load in the presence of cracks properly, however they used the homogeneous solution mainly to correlate l_c to the materials intrinsic strength only (Alessi et al., 2018; Amor et al., 2009; Benallal and Marigo, 2006; Borden et al., 2012; Frémond and Nedjar, 1996; Lorentz and Andrieux, 2003; Mesgarnejad et al., 2015; Nguyen et al., 2016a; Pham et al., 2011; Pham and Marigo, 2010a,b; Pham et al., 2017; Tanné et al., 2018). Their work was not extended to explain the transition and eventually the size effect using a simple mechanical theory.

This paper aims for a nuanced and deepened understanding of the elementary mechanism introduced by the phase-field approximation. We draw a comparison between the variational approach and the so-called coupled criterion (Leguillon, 2002). The latter was one of the first theories to give an elegant and straightforward explanation of the well-known size effect. Therefore, we consider this analogy essential because, according to the authors' best knowledge, this mechanism in phase-field simulations has never been fully explained.

Finite fracture mechanics, and particularly the coupled energy- and stress-based criterion proposed by Leguillon (2002), allows the prediction of crack initiation in various materials and configurations. The theory postulates that both criteria are necessary conditions to calculate the critical load, but neither one is sufficient on its own. It has been successfully employed for the failure of ceramics (Leguillon et al., 2018; Martin et al., 2018), composites (Doitrand et al., 2017; García et al., 2018; Martin et al., 2012), notched specimens (Cornetti et al., 2013; Leguillon et al., 2007) and bi-material interfaces (Doitrand and Leguillon, 2018b; Mantič, 2009; Stein et al., 2015). A detailed review of the applications can be found in the work of Weißgraeber et al. (2016). More recent works include its extension to 3D cases (Doitrand and Leguillon, 2018a,c; García et al., 2016; Yosibash and Mittelman, 2016), nonlinear materials (Doitrand and Sapora, 2020; Leguillon and Yosibash, 2017; Li et al., 2019; Rosendahl et al., 2019), 3D-printed polymers (Xu and Leguillon., 2019), fatigue limit prediction (Liu et al., 2020) or its coupling to the peridynamics approach (Zhang and Qiao, 2018).

When satisfying both criteria, a length emerges, which might be a related quantity to the length scale used in diffuse damage approaches. The coupled criterion has already been successfully compared to other methods, such as the CZM (Cornetti et al., 2019, 2016; Doitrand et al., 2019; García et al., 2014; Henninger et al., 2007; Martin et al., 2016; Poitou et al., 2007), and the TLS (Zghal et al., 2018) approach. Generally, the papers conclude that the qualitative correlation is good if the characteristic lengths of the geometry (specimen size, initial crack length, crack tip radius) are much larger than the size of the PZ. However, the results start to deviate if these quantities are of the same magnitude. Both methods are capable of determining critical loading states, which can be calibrated to reproduce the experimental results. Furthermore, Doitrand et al. (2019) showed that not only the traction-separation limit but also the function's profile has a significant effect on the results, especially concerning crack initiation. In conclusion, even if these authors

compared the two methods, a universal explanation for the size effect introduced by the regularization length is still missing in phase-field methods.

We aim to deepen the comparison and to assess the similarities in the phase-field method between the critical loads, crack topology, and arrest length in unstable-stable crack initiation cases. This analysis will provide an insight to explain the effect of the length scale parameter on the mechanical behavior of the materials.

The present paper is structured as follows. Section 2 introduces the two principal methods - the phase-field damage model and the coupled criterion - used to study brittle fracture. After a summary of the theoretical background, a failure envelope based on the homogeneous phase-field solution is introduced, and the main results are outlined in section 3. In each case, the obtained correlation between the tensile strength and the length scale parameter is highlighted. Section 4 is dedicated to assessing the differences between the coupled criterion and the diffuse damage models. Finally, section 5 concludes the paper.

2. Methods

This section introduces the two methods used to model brittle fracture in the present work. First, the phase-field approach is outlined after which the foundations of the coupled criterion are presented. Thanks to the rich literature on both methods, we here only give a short overview, which is essential in order to understand their comparison, but we will not enter into details.

2.1. Phase-field approach for brittle fracture

The phase-field approach utilized to model a fracture is based on the diffuse representation of the localized discontinuity. The crack surface is approximated with a damage variable (d) ranging from 0 to 1. If the phase-field is 0, the domain is undamaged, while if its value reaches 1, the crack is emerged, and the material lost all of its resistance and stiffness. Various phase-field models can be found in literature (Ambati et al., 2015b; Wu, 2018b). The principal differences lay in the so-called geometric crack function and the elastic energy degradation function. One of the earliest and most widely used approach assumes that the damage enters the equation of the crack surface density in a quadratic manner (Bourdin et al., 2000b; Miehe et al., 2010a):

$$W(d) = g_c \Gamma(d) = \int_\Omega g_c \gamma(d, \nabla d)\, d\Omega = \int_\Omega \frac{g_c}{2 l_c} \left[d^2 + l_c^2 |\nabla d|^2 \right] d\Omega \tag{1}$$

where Γ is the overall crack surface, and g_c is the critical energy release rate defined by Griffith. The sharp discontinuity is replaced by a smeared representation of the surfaces by the integration of γ, the crack surface density, which is calculated using the length scale parameter l_c, which eventually controls the size of the regularization zone.

This representation has many advantages, therefore it is possibly one of the most commonly used. The solution algorithm can be coded in a standard finite element solver, when l_c goes to 0, the fracture surface converges to the theoretical Griffith limit, and the natural bonds of the damage ($0 \leq d < 1$) is automatically satisfied. One of its major flaws is that due to the quadratic setting it does not have an initial elastic threshold. Some authors tried to correct this flaw by adding an initial elastic threshold (Miehe et al., 2016; Molnár et al., 2020; Wu and Huang, 2020), however in all of the cases the crack surface calculated from the damage topology overestimates the theoretical value by more than 20%, which makes this method somewhat unreliable. On the other hand Pham et al. (2011) proposed a description with the damage variable entering the surface only with a linear term. With this crack function the stress remains elastic until fracture, however without special treatment the natural lower bond of the damage variable is violated ($d < 0$). Thus, the solution of the problem requires a bonded non-linear optimization algorithm, which is hardly implemented in most of the commercial finite element codes, such as Abaqus. Wu (2018b) proposed a mixture of the two worlds, which renders a CZM like representation, however in their case, the strength is an explicit material parameter, thus independent of the length scale. Therefore, this formulation is inappropriate for this study. As a conclusion, even if the quantitative comparison would change with the chosen phase-field formulation, the main findings of this paper would remain qualitatively the same. For a general overview of the available phase-field formulations we refer to the work of Ambati et al. (2015b).

The damage variable and the strain energy density (ψ) are connected through the degradation function:

$$\psi(\boldsymbol{\varepsilon}, d) = g(d)\, \psi_0^+(\boldsymbol{\varepsilon}) + \psi_0^-(\boldsymbol{\varepsilon}). \tag{2}$$

The elastic strain energy (ψ_0) is split into positive (extension) and negative (compression) components based on the principal strains (ε_i) and the trace of the strain tensor:

$$\psi_0^{+,-}\left(\hat{\boldsymbol{\varepsilon}}\right)=\sum_i \mu\langle\varepsilon_i\rangle_{+,-}^2+\frac{\lambda}{2}\langle tr\left(\boldsymbol{\varepsilon}\right)\rangle_{+,-}^2, \tag{3}$$

where λ and μ are the Lamé parameters. To distinguish between compression and extension, positive and negative part functions are used. Equation (2) indicates that if the material is in tension, the tensile stiffness and the elastic stress are reduced with the damage variable. Present implementation uses the well-known quadratic degradation function: $g\left(d\right)=\left(1-d\right)^2$.

The solution for the displacements ($\mathbf{u}$) and the phase-field (d) problem is obtained by minimizing the following energy functional in a staggered manner:

$$\mathcal{L}=\Pi^{\text{int}}\left(\mathbf{u},d\right)+W\left(d\right)+T\left(d\right)-\Pi^{ext}, \tag{4}$$

with the internal and external strain energies defined as follows:

$$\begin{aligned}&\Pi^{\text{int}}\left(\mathbf{u},d\right)=\int\limits_{\Omega}\left[g\left(d\right)\psi_0^{+}\left(\boldsymbol{\varepsilon}\left(\mathbf{u}\right)\right)+\psi_0^{-}\left(\boldsymbol{\varepsilon}\left(\mathbf{u}\right)\right)\right]d\Omega,\\&\Pi^{ext}=\textstyle\int_{\Omega}\overline{\boldsymbol{\gamma}}\cdot\mathbf{u}dV+\int_{\partial\Omega}\overline{\mathbf{t}}\cdot\mathbf{u}dA.\end{aligned} \tag{5}$$

where $\overline{\boldsymbol{\gamma}}$ and $\overline{\mathbf{t}}$ are external volumetric and boundary forces.

The monolithic solution of the fully coupled problem suffers from convergence issues, therefore Miehe et al. (2010b) decoupled the two solutions by introducing a history field ($\mathcal{H}$). In one iteration step, the damage and $\mathcal{H}$ are kept constant for the mechanical and the phase-field problem, respectively:

$$\mathbf{u}_{n+1}=\text{Arg}\left\{\inf_{\mathbf{u}}\int_{\Omega}\left[\psi\left(\mathbf{u},d\right)-\bar{\boldsymbol{\gamma}}\cdot\mathbf{u}\right]dV-\int_{\partial\Omega}\overline{\mathbf{t}}\cdot\mathbf{u}dA\right\}, \tag{6}$$

$$d_{n+1}=\text{Arg}\left\{\inf_{d}\int_{\Omega}\left[g_c\gamma\left(d,\nabla d\right)+\left(1-d\right)^2\mathcal{H}\right]dV\right\}, \tag{7}$$

with the history variable chosen as:

$$\begin{aligned}&\mathcal{H}_0=0,\\&\mathcal{H}_{n+1}=\max\left\{\begin{array}{c}\psi_0^{+}\\\mathcal{H}_n\end{array}\right\}.\end{aligned} \tag{8}$$

This formation satisfies the Karush–Kuhn–Tucker conditions (Singh et al., 2016).

Unfortunately, there is no detailed mathematical proof that the introduction of the history variable enforces damage irreversibly, therefore we explicitly enforced $\dot{d}\geq 0$ in the displacement element. However, we have not observed that this criterion was violated more than the numerical precision during our simulations. Though there are other methods to obtain a positive damage rate (*e.g.,* bound constrained non-linear optimization techniques (Amor et al., 2009; Farrell and Maurini, 2017; Wu, 2018b), augmented Lagrangian (Lorentz and Godard, 2011; Wheeler et al., 2014) or penalization methods (Gerasimov and Lorenzis, 2019)), due to its simplicity the history field of Miehe et al. (2010b) is the most frequently used (Wu and Huang, 2020). More details about the Abaqus implementation can be found in our previous papers (Molnár and Gravouil, 2017; Molnár et al., 2020).

To demonstrate how the damage variable affects the stress response, the homogeneous solution is calculated by neglecting the gradient of the damage variable (∇d). The maximum tensile stress is plotted in Fig. 1(a) as a function of the applied tensile strain for a unidirectional extension case. The horizontal displacement is fixed, and the top side is moved upwards. Fig. 1(b) shows the evolution of the damage as a function of the applied deformation.

The tensile strength (σ_c) of a material is defined as the maximum amount of tensile stress ($\sigma^{\max}$) that it can withstand before failure. When the gradient is neglected the homogeneous solution for the tensile strength can be obtained from the material parameters by the following equations: $\sigma^c=\sqrt{\frac{27Cg_c}{256l_c}}$ in unidirectional extension, where $C=\frac{E(1-\nu)}{(1+\nu)(1-2\nu)}$ in which E is Young's modulus and ν is Poisson's ratio. The relationship can be generalized:

$$\sigma^c\doteq\sigma^{\max}=\eta\left(\nu,\frac{\sigma_2}{\sigma_1}\right)\cdot\sqrt{\frac{Eg_c}{l_c}}, \tag{9}$$

where the function η takes the effect of the stress state and the effect of Poisson's ratio into account. Fig. 1(c) shows the evolution of the maximum stress in the space of the principal stresses for the 2D case.

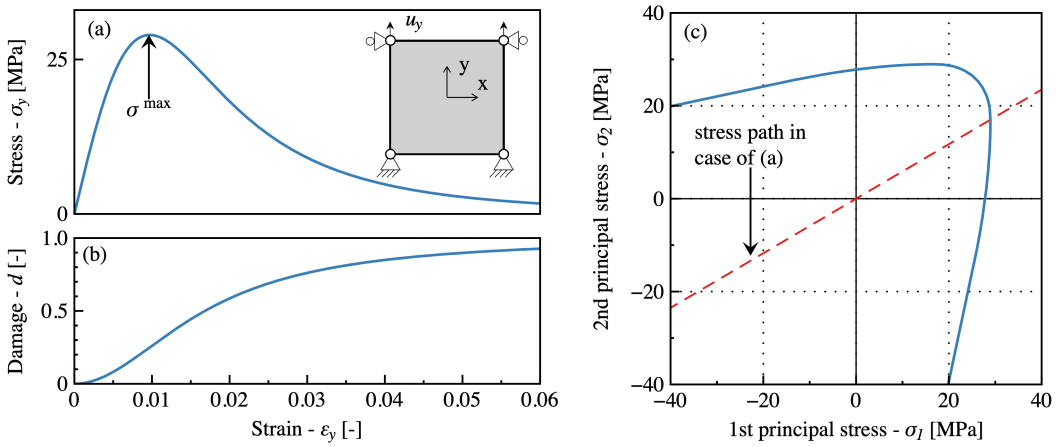

Figure 1: Homogeneous solution of the phase-field problem in unidirectional tension: (a) stress-strain curve; (b) damage as a function of the applied deformation; (c) failure envelope (maximum stress states) in the space of principal stresses. The stress path in the case of part (a) is depicted using a dashed line. The results were obtained with $E = 3$ GPa, $\nu = 0.37$, $g_c = 300$ J/m^2 and $l_c = 0.2$ mm.

Details of the homogeneous solution are given in Appendix A with a MATLAB algorithm in the Supplementary Materials to calculate the tensile strength for a given material. When E, ν, g_c and l_c are known, the strength can be determined. In the opposite case, when searching for an applicable l_c, σ_c can be measured experimentally, and the algorithm can be used to determine a regularization length for the phase-field simulation.

One of the earliest attempt to quantify a length scale in fracture was proposed by Irwin (1958). We call l_{mat} the materials intrinsic length[1]:

$$l_{mat} = \frac{E g_c}{\sigma_c^2}. \tag{10}$$

The correlation between the length scale used in phase-field fracture and l_{mat} is given by the function η:

$$l_c = \eta^2 \cdot l_{mat}. \tag{11}$$

This relationship was shown for unidirectional tension by Tanné et al. (2018), however no correlation was given between these internal lengths and the actual size of the process zone. Therefore, the question remains open still today if there is a general correlation between these intrinsic quantities – deduced based on the strength and the toughness – and the length of the crack upon initiation.

2.2. Coupled stress and energy criterion

The coupled criterion is an elegant tool used in finite fracture mechanics. This approach combines an energy condition with a stress-based comparison. For a crack to propagate, both criteria have to be satisfied at the same increment length. The energy release rate (G) is determined through a balance between the states before and after the crack jump. In most cases, the phononic dissipation is neglected, and quasi-static conditions are assumed. In order to calculate the energy release rate, two options are thus presented.

The first is called the incremental value, where G is considered constant during the initiation and propagation:

$$G_{inc}(a_0 + \Delta a, P) = -\frac{\Pi^{int}(a_0 + \Delta a, P) - \Pi^{int}(a_0, P) + \Delta\Pi^{ext}(F, u)}{\Delta a} \geq g_c, \tag{12}$$

where G_{inc} is the incremental energy release rate, Π is the elastic strain energy, and P represents the applied displacements (u) or external forces (F) on the boundaries. It reverts to the Griffith definition of the energy release rate when

[1] E is usually replaced by an equivalent stiffness to account for different loading cases. In this paper we consider that l_{mat} is only the ratio of the three material constants above and the stress state is accounted for via η. This allows us to precisely distinguish between l_c and l_{mat}.

the incremental crack length tends towards $\Delta a \to 0$. Here, a_0 is the initial crack length, and Δa is the unknown crack increment.

The second approach assumes that the energy release rate varies during the propagation. Consequently, G can be derived as:

$$G(a_0 + \Delta a/2, P) = -\frac{\partial \Pi\left(a_0 + \Delta a/2, P\right)}{\partial a} \approx -\frac{\Pi^{int}(a_0 + \Delta a, P) - \Pi^{int}(a_0, P) + \Delta\Pi^{ext}\left(F, u\right)}{\Delta a} \geq g_c. \tag{13}$$

In practice, the incremental approach is used when there is no initial crack (*e.g.,* only a V-notch exists), and the initiation is considered instantaneous (Leguillon, 2002). The second, on the other hand, is more suitable if there is already a sharp crack present. Usually, the second criterion gives a lower propagation length and initiates at a smaller loading. However, when $\Delta a \to 0$, the incremental value converges to the differential G. In this paper, we present an analysis of the results from both descriptions.

The second requirement of the propagation is given by the stress criterion. We assume that the elastic stress around the crack tip along the expected crack path (described by its curvilinear abscissa s) is higher than the material's tensile strength:

$$\sigma_t\left(a + s, P\right) \geq \sigma_c, \forall\ 0 \leq s \leq \Delta a, \tag{14}$$

Here, σ_t is the stress perpendicular to the crack's opening direction (tangential). Usually, for a tensile case, in homogeneous and isotropic materials, this is equivalent to the first principal stress.

Interestingly for the stable initiation, both energy and stress functions decrease monotonously with the advancement of the crack. Therefore, the energy release rate determines the initiation state. For an unstable initiation, on the other hand, the energy criterion is defined by an increasing function, and the stress criterion by a decreasing one.

As a result, the energy criterion provides a minimum crack length, and thus a lower bond, from which the condition is satisfied. However, due to the singularity at the tip, the stress criterion will provide a maximum distance, thus an upper bond for the admissible initiation crack length.

In order to satisfy both criteria simultaneously, the load is increased so that the initiation length provided by the energy criterion decreases until it matches its value given by the distance along the crack path on which the stress criterion is satisfied. A main conclusion of the coupled criterion is thus that a finite crack length Δa is abruptly created at initiation so as to satisfy both the strength and energy requirements. Consequently, the coupled criterion allows us to determine the loading P_c when the crack initiates:

$$P_c = min\left(P, \exists \Delta a, min\left(\frac{G(a_0 + \Delta a, P)}{g_c}, \frac{\sigma(a_0 + \Delta a, P)}{\sigma_c}\right) \geq 1\right), \tag{15}$$

as well as the admissible initiation lengths Δa_c:

$$\Delta a_c = \{\Delta a, min\left(\frac{G(a_0 + \Delta a, P_c)}{g_c}, \frac{\sigma(a_0 + \Delta a, P_c)}{\sigma_c}\right) \geq 1\}. \tag{16}$$

In practice, the energy release rate and the stress fields can both be obtained analytically or by using the finite element method. Under the assumption of small deformations and in a linear elastic framework, only one linear elastic calculation is needed to compute the stress condition, whereas computing the energy criterion requires some linear elastic calculations with varying crack length.

3. Results

Progressively, through benchmark examples, the similarities, the differences, and the correlation between tensile strength and length scale are highlighted. In the case of the simple extension (mode I) discussed in Section 3.1, the energy release rate, the stress fields, and the crack path are all available analytically. For a shear fracture presented in Section 3.2, on the other hand, only parts of the necessary fields are known. To determine the initiation angle, we mapped the region around the crack tip to determine the energy release rate using the finite element method. Finally, in our last example shown in Section 3.3, a finite-size specimen was studied with particular attention to the initiation and arrest lengths.

In all cases, the material was considered isotropic and homogeneous with the material constants shown in Tab. 1. The tensile strength (σ_c) and length scale (l_c) parameters were varied.

Material constant	
Young's modulus (E)	3 GPa
Poisson's ratio (ν)	0.37
Critical energy release rate (g_c)	300 J/m^2

Table 1: Material constants used in the calculations.

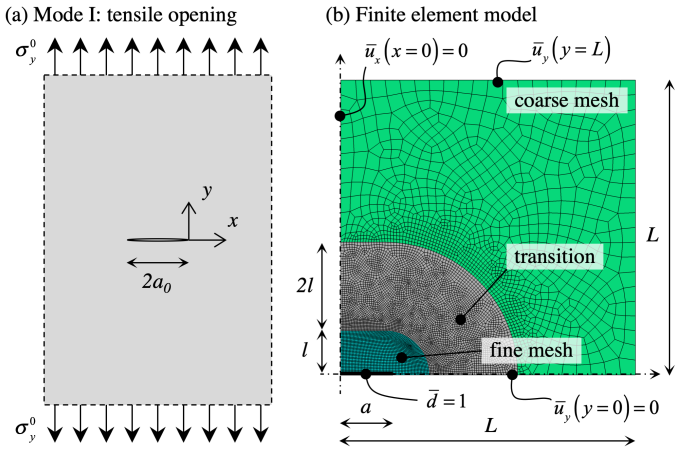

Figure 2: Mode I tensile opening: (a) schematic problem; (b) finite element model with double symmetry . $L = \max(10a, 20\text{mm})$. For the phase-field calculation, only the intact horizontal part was constrained against u_y, the crack faces were left free to move.

The cracks were represented both physically and with prescribed phase-field values. In case of the examples presented in Section 3.1 and 3.3, due to the symmetry, only one quarter and one half of the geometry was modeled respectively. Thus, the connecting symmetry line was constrained in the parallel direction, while the crack faces were left free to displace. In case of the shear example (presented in Section 3.2) the nodes were doubled to physically represent the initial fracture. This was reported (Strobl and Seelig, 2020) to be essential because of the energy decomposition applied (see eq. 2). In both cases Dirichlet boundary conditions were prescribed on the crack faces in the phase-field ($d = 1$) which represented an already nucleated crack (Klinsmann et al., 2015; Sargado et al., 2018; Tanné et al., 2018).

3.1. Mode I tensile opening in an infinite plane

Coupled criterion. Griffith (1921) first proposed the energy-based criterion to study a single straight crack in an infinite homogeneous plane subjected to uniform tensile stress applied in the plane at the outer edge. To compare analytical results with the phase-field solution, we chose a "thick" plate, that is to say plane strain conditions.

The schematic illustration of the problem is depicted in Fig. 2(a). For the **coupled criterion** the stress can be calculated on the (Ox) axis ($y = 0$) measured from the crack tip with the following equation (Sun and Jin, 2012):

$$\sigma_y(x) = \frac{\sigma_y^0 (x + a_0)}{\sqrt{x(x + 2a_0)}}, \tag{17}$$

where a_0 is the initial crack length and σ_y^0 is the tensile stress acting on the solid body at infinity.

From this equation, we can measure the distance from the crack tip, where the stress exceeds the tensile strength:

$$\Delta a^\sigma = a_0 \left[\frac{1}{\sqrt{1 - \left(\sigma_y^0/\sigma_c\right)^2}} - 1 \right]. \tag{18}$$

Using similar algebraic manipulations, the admissible crack increment defined by Griffith's energy criterion (Griffith, 1924) can be expressed. The criterion is written as a stability condition:

$$\frac{d}{da}\left(S-\Pi\right)=0, \tag{19}$$

where Π is the additional elastic strain energy induced by the crack:

$$\Pi=\frac{\pi(a_0+\Delta a)^2}{8\mu}\left(\kappa+1\right)(\sigma_y^0)^2, \tag{20}$$

and S is the fracture energy consumed by the creation of the crack:

$$S=2g_c\left(a_0+\Delta a\right). \tag{21}$$

In eq. (20), μ is the shear modulus and $\kappa=3-4\nu$ for the plane strain case. Eq. (19) can be rewritten as:

$$G=\frac{\pi\left(a_0+\Delta a\right)}{8\mu}\left(\kappa+1\right)(\sigma_y^0)^2=g_c, \tag{22}$$

from which criterion the critical crack increment can be expressed as:

$$\Delta a^G=\frac{8g_c\mu}{\left(\kappa+1\right)\pi\left(\sigma_y^0\right)^2}-a_0. \tag{23}$$

The obtained result can be reformulated to determine the maximum loading stress as a function of an already existing crack (a_0):

$$\sigma_y^{0,G}=\sqrt{\frac{8g_c\mu}{\left(\kappa+1\right)a_0\pi}} \tag{24}$$

This stress value can be considered as an upper bond for the critical loading.

If we assume that the crack can propagate only until the point where the stress exceeds the strength, and can only be opened if there is enough potential energy released, the critical applied stress can be defined ($\Delta a^\sigma=\Delta a^G$) as follows:

$$\sigma_y^{0,c}=\sigma_c\sqrt{\frac{2}{1+\sqrt{1+\sigma_c^4\frac{\pi^2a_0^2(1+\kappa)^2}{16g_c^2\mu^2}}}}=\sigma_c\sqrt{\frac{1}{\frac{1}{2}+\sqrt{\frac{1}{4}+\left(\frac{\sigma_c}{\sigma_y^{0,G}}\right)^4}}}, \tag{25}$$

It is worth noting that the critical load is a function of not only the strength and the fracture toughness but the geometry (initial crack length) as well. Thus, with the above equation, a size effect can also be captured, which will be discussed later.

To demonstrate the evolution of the two criteria, the normalized values are depicted in Fig. 3. It can be seen that initially, at low loading values, Δa^σ (crosses) is much smaller than Δa^G (circles). However, the gradual increment of σ_y^0 brings the two values closer until they match. This length (Δa) is considered the initiation of the crack.

$$\frac{G}{g_c}=\frac{\sigma_y}{\sigma_c}\geq 1.0. \tag{26}$$

In our case, this only happens if $\sigma_y^0\geq\sigma_y^{0,c}$.

Equation (25) is the analytical solution for the maximum homogeneous stress, which can be applied based on the coupled criterion. The instantaneous initiation length (Δa_c) can be determined by substituting the critical stress in eq. (25) into either eq. (18) or (23). Fig. 6(b) shows Δa_c as a function of the initial crack length.

Phase-field. To model the same problem using the phase-field approach, a geometry shown in Fig. 2(b) was used. Only one quarter of the space was taken into account with symmetric boundary conditions on the middle lines. The overall length of the sample (L) was taken larger than $100a$, otherwise the finite size had a marked effect on our results. Dirichlet boundary conditions were prescribed on the edges as displacements and a $d=1$ phase-field value on the crack surface. The prescribed phase-field value was shown to be necessary as the creation of the crack required more energy than the propagation of an already existing damage field (Klinsmann et al., 2015; Sargado et al., 2018; Tanné et al., 2018).

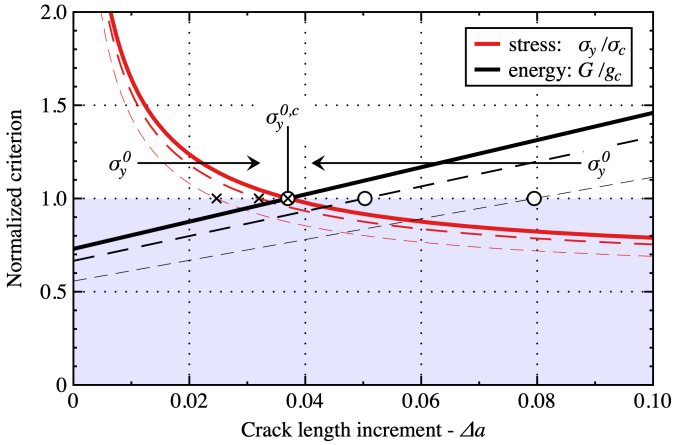

Figure 3: Coupled stress and energy criteria for tensile (mode I) fracture. Black crosses represent the length where the stress criterion is just satisfied, while hollow circles show the same for the energy release rate. By increasing the external load, the two positions approach each other until both are satisfied.

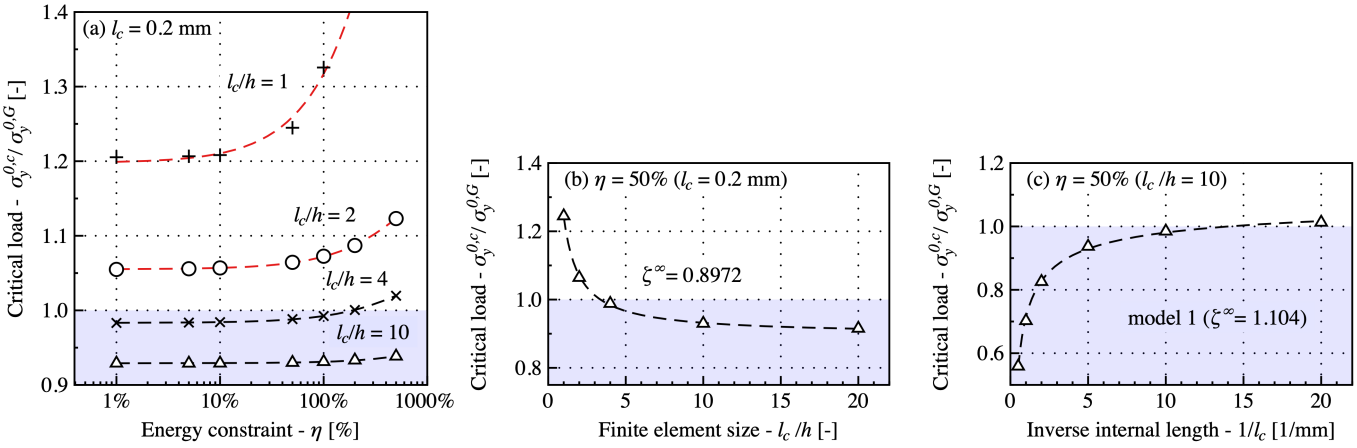

Figure 4: Convergence analysis of the phase-field simulation for tensile (mode I) fracture with an initial crack length of $a = 2$ mm. The applied critical stress ($\sigma_y^{0,c}$) is shown normalized by Griffith's solution ($\sigma_y^{0,G}$). (a) Results as a function of the maximal energy increment (η) and the finite element sizes with constant $l_c = 0.2$ mm. The dashed curves are guides for the eye. (b) Critical stress as a function of the finite element size for different models with $l_c = 0.2$ mm. A hyperbolic curve ($\zeta^\infty + \xi \frac{h}{l_c}$) with a convergence to ζ^∞ (at $l_c/h \to \infty$) is fitted to the data. (c) Critical stress as a function of l_c with an inverse square root function ($\zeta^\infty + \xi\sqrt{l_c}$), where $l_c \to 0$ the value converges to ζ^∞. The goodness-of-fit of all functions was greater than $R^2 > 0.99$.

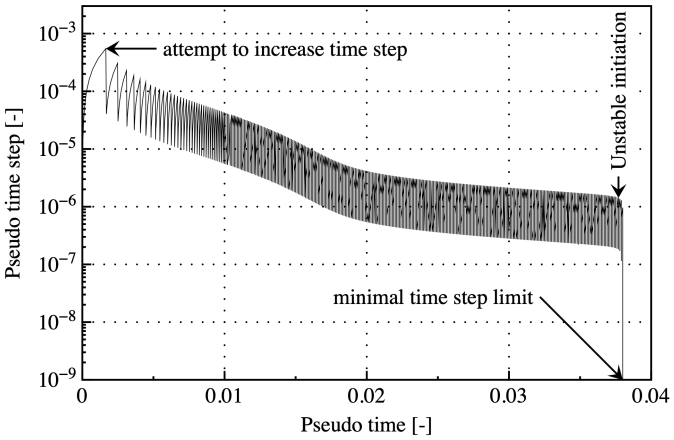

Figure 5: Chosen time step during the simulation with $\eta = 0.5$ and $l_c = 0.1$ mm.

Recently Kumar et al. (2020) proposed an additional crack driving force attributed to microscopic damage to account for the correct nucleation phenomenon.

The material properties were set according to Tab. 1.

The results obtained using the finite element, and thus, the phase-field method, were affected by both the spatial and temporal discretization. Therefore, a convergence study was carried out to minimize the error induced by the numerical approach.

The time step was controlled automatically. The local potential energy increment was constrained based on the following condition:

$$d\mathcal{H} \leq \eta \cdot \frac{g_c}{2l_c}, \tag{27}$$

where $\mathcal{H}$ is the elastic (undamaged) strain energy history used in the staggered schemes (Miehe et al., 2010b; Molnár and Gravouil, 2017; Molnár et al., 2020) and η is a scalar multiplier. There are other methods to determine an optimal time step size. We chose to constrain the elastic energy because Abaqus solves the displacement and fracture problems simultaneously. Therefore, the control of the fracture energy is not tractable. For a general overview, we refer to the work of Gupta et al. (2020).

In Fig. 4(a), the normalized critical stress values are shown as a function of η for different finite element mesh densities. It can be seen that by constraining the local elastic energy increment, the critical load decreased, and the precision of the simulations improved. If an $\eta \leq 50\%$ was chosen, the critical stress changed by less than 0.1%.

Similarly to the temporal discretization, the spatial mesh also had a significant effect on the results. Miehe et al. (2010a) proposed a ratio of $l_c/h = 2$ value based on the crack surface. However, as shown in Fig. 4(b), the mechanical effect changed notably until $l_c/h = 10$.

Finally, to find out if the phase-field solution converged to the theoretical Griffith value, l_c was reduced. The other two numerical parameters were kept at $\eta = 50\%$ and $l_c/h = 10$. It can be seen in Fig. 4(c), that the solution converged to a value $\approx 10\%$ higher than $\sigma_y^{0,G}$, which could supposedly be reduced by increasing the finite element density and reducing the time step.

Thus, if not otherwise stated, the simulations are performed using $\eta = 50\%$ and $l_c/h = 10$ with varying l_c.

In Fig. 5 the variation of the time step is shown for $l_c = 0.1$ mm with $\eta = 0.5$. After an increment the algorithm gradually decreased the critical time step size to $\approx 10^{-6}$ until the loading reached the unstable initiation stage. The fluctuations show that the time integration algorithm of Abaqus continuously tried to increase the time step to accelerate the calculation. At the moment of an unstable initiation the time is reduced close to zero ($\approx 10^{-9}$). With the adaptive time integration algorithm we were able to detect unstable initiation and avoid the error described by Ambati et al. (2015b).

One of the main advantages of the coupled criterion is that it can capture an experimentally well-observed size effect. Bažant (1999) showed that the fracture resistance of several materials (even glasses (Kimoto et al., 1985)) deviated from the power-law described by linear elastic fracture mechanics (LEFM). This was particularly true if the initial flaw size

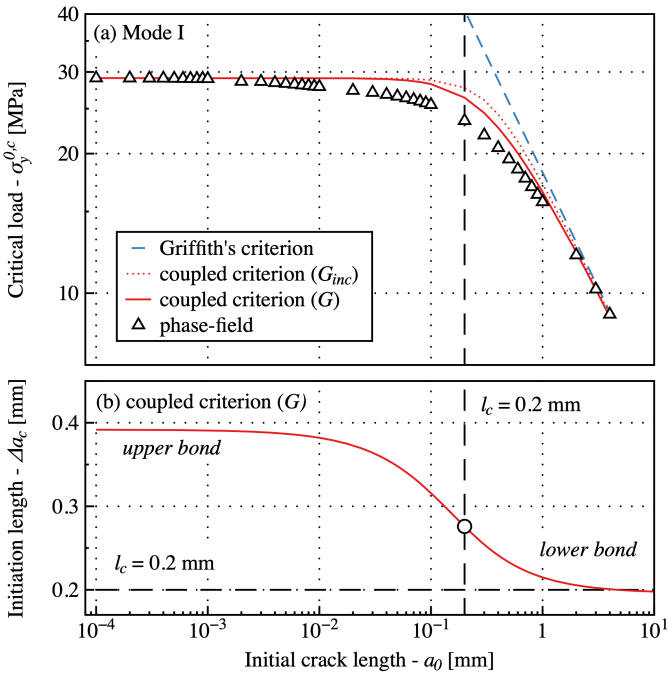

Figure 6: (a) Critical stress obtained by phase-field simulations (symbols) and the coupled criterion (red curves) as a function of the initial crack length in mode I fracture. With blue dashed line the solution of Griffith is plotted. The length scale parameter used in the phase-field simulations are highlighted at $a = l_c = 0.2$ mm. (b) Initiation length as a function of the initial crack length calculated using the coupled criterion and eq. (13).

was smaller than a critical value. In this case, the verification should be carried out based on a stress comparison. Since Bažant (1999), multiple authors proposed a unified description applying the coupled criterion for ceramics (Leguillon et al., 2018; Martin et al., 2018), PMMA and GPPS (Doitrand and Sapora, 2020; Sapora et al., 2018), which follows the experimentally observed size effect.

Fig. 6 presents a plot of a similar size effect as a function of the initial crack length. Critical stresses are shown as a function of the initial crack length using the coupled criterion (see eq. 25) with red curves, the original Griffith solution (see eq. 24) with a blue dashed line and phase-field simulations with black symbols. The tensile strength used in the coupled criterion was taken according to the critical stress value obtained at a very small crack length ($a = 10^{-4}$ mm) in the phase-field simulations.

It can be seen that the phase-field results were capable of reproducing the same size effect as was theorized and experimentally measured before. Furthermore, the deviation from LEFM started when the initial crack size approached and became smaller than l_c. In Fig. 6(b) the initiation length (Δa_c) varies between l_c and $2l_c$ with an inflection point at $a_0 = l_c$. This result indicates that the correlation between l_c and the size of the process zone is not unique because, depending on the initial crack length, its value varies. Nevertheless, the two quantities are on the same scale. Later in Section 4 the correlation between l_c and Δa_c will further be discussed.

Additionally, it can be seen that the phase-field results were closer to the instantaneous description of G since the deformation field was allowed to evolve and change with the advancement of the crack during the simulation. Nevertheless, there was a small difference between the critical stress results, which might be due to the fact that the coupled criterion uses an infinite stress field, while the singularity in the phase-field model is regularized. This discrepancy is discussed in section 4.

The results presented in Fig. 6 are critical as they show that the introduction of the crack diffusion, and thus the length scale, does not spoil the original description of Griffith but adds a unique tool to capture the real-life physical phenomenon. Even if the choice of the phase-field description affects the behavior of the models, it is essential to consider that l_c possesses a real mechanical meaning.

Multiple computations were carried out with $a = 0$ in the phase-field calculation to determine a correlation between tensile strength and the length scale. This way, the initial damage field was prescribed only on a single node. As explained

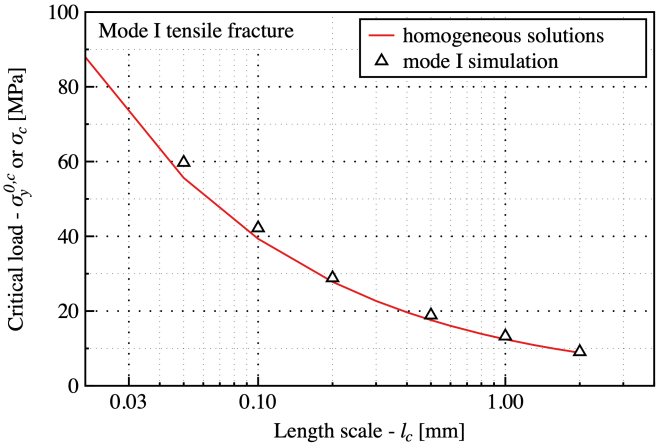

Figure 7: Critical stress as a function of l_c with different models for mode I tensile opening for $a = 0$ obtained using phase-field simulations and the homogeneous solution for unidirectional tension (based on eq. 9).

previously, in this case, the critical initiation stress corresponded to the material's strength, hence allowing for a direct comparison for several length scales in the phase-field method. The critical stress results were recorded as a function of the l_c used. In Fig. 7, the obtained σ_c-l_c pairs are shown with the homogeneous solution from eq. (9) for uniaxial tension (with the principal stress ratio of $\sigma_2/\sigma_1 = 0$).

There is a clear correlation between the two quantities. By decreasing l_c, the tensile strength is raised and tends to infinity. This result is in agreement with the original solution by Griffith, since when $a \to 0$, $\sigma^{0,G}$ tends to infinity.

3.2. Mode II shear fracture

After assessing the critical stress for the two methods as a function of the initial crack length, this section focuses on the crack's topology. For mode II shear fracture, the prediction of the initiation angle is still an unsolved question. Many theories have been proposed, based on the maximum tangential stress (Erdogan and Sih, 1963), the strain energy density (Sih, 1974), the energy release rate (Hayashi and Nemat-Nasser, 1981; Wu, 1978), or even the stress intensity factors (Amestoy and Leblond, 1992; Leblond, 1989). Some of them reproduce specific experiments (Erdogan and Sih, 1963), but none of them can describe a universal law that is valid for all materials (Ayatollahi and Aliha, 2009; Richard et al., 2014).

We assume that the variation in initiation comes from the difference in regularization length, thus the ratio of strength and toughness. Therefore, we set out to analyze the initiation using both the coupled criterion and the phase-field method and establish a correlation based on the quantity above.

Fig. 8(a) shows the theoretical problem of mode II shear fracture. The applied shear stresses acted on the sides at infinity. The initiation angle θ was measured from the horizontal axis.

Experimentally, Ayatollahi and Aliha (2009) tried to model pure shear on a finite-size specimen by maintaining an angle between the pulling forces and the initial crack, as shown in Fig. 8(b). However, we show later on using a phase-field model that their geometry has a significant effect on the initiation angle, and that the two cases are not equivalent.

Coupled criterion. Unfortunately, no analytical solutions were available to test the coupled criterion on a mode II fracture. Only certain aspects of the stress and energy field were known. The elastic stress field around the initial crack tip is described in various textbooks (Broek, 1982; Sun and Jin, 2012), whereas the energy release rate is given only for the case when $\theta = 0$ (Broek, 1982):

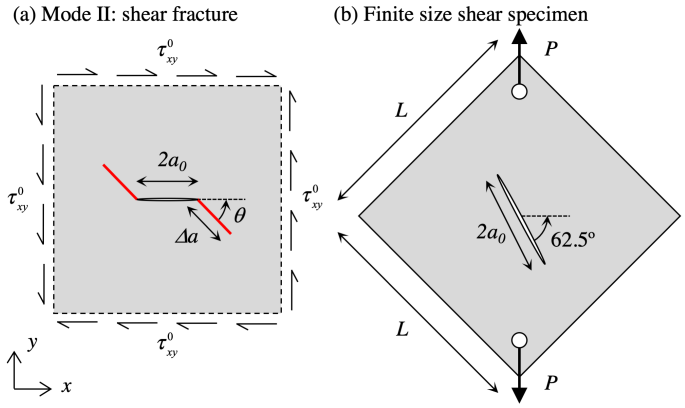

Figure 8: Mode II shear test: (a) schematic illustration of the problem in an infinite domain; (b) diagonally loaded square plate (with finite-size) for experimental comparison: $L = 150$ mm, $2a_0 = 45$ mm.

$$
\begin{aligned}
G\left(\Delta a, \theta = 0\right) &= \lim_{\Delta a \to 0} \frac{\Delta \Pi\left(\Delta a, \tau_{xy}\right)}{2\Delta a} \\
&= \lim_{\Delta a \to 0} \frac{\Pi\left(a_0 + \Delta a, \tau^0_{xy}\right) - \Pi\left(a_0, \tau^0_{xy}\right)}{2\Delta a} \\
&= \frac{\pi\left(\kappa + 1\right)\left(\tau^0_{xy}\right)^2}{8\mu} \lim_{\Delta a \to 0} \left(\frac{a_0^2 - \left(a_0 + \Delta a\right)^2}{2\Delta a} \right) \\
&= \frac{\pi\left(\kappa + 1\right)\left(\tau^0_{xy}\right)^2}{8\mu} \left(a_0 + \Delta a\right) \\
&\geq g_c,
\end{aligned}
\tag{28}
$$

and for the case when $\Delta a = 0$ by Wu (1978) and Hayashi and Nemat-Nasser (1981).

For this reason, we carried out the following modeling strategy to obtain a precise close crack tip ($\Delta a < a/2$) solution: First, finite element calculations were performed with varying crack length values in different directions ($-90° \leq \theta \leq 0$), after which the global energy difference was calculated between each crack increment (see eq. 13). Finally, we used empirical functions to fit the results.

The calculation of the energy release rate using finite elements is relatively straightforward. To minimize the size effect, the overall size of the plate was $L = 250a_0$. As boundary conditions, we used distributed shear forces in the boundaries. G was computed between energy values calculated for the same θ value with increasing Δa. Between each model the crack was increased by $\delta a = 0.025a_0$. To eliminate the fluctuation caused by the mesh the so-called seam crack was utilized. Practically, the same finite element mesh was used independently of the crack size, and only the nodes were doubled on the crack lips to separate the elements. This technique makes it possible for us to use the same mesh, for a constant θ value, and to significantly reduce the fluctuation in the energy release rate. The characteristic element size around the crack was set to $\delta a/100$.

The maximum difference between finite element calculations and available analytic data was less than 1%, which means they were of the same order of the magnitude. In order to speed up the calculation, a continuous function was fitted:

$$
G\left(\Delta a, \theta\right) = \frac{a_0 \pi\left(\kappa + 1\right)\left(\tau^0_{xy}\right)^2}{8\mu} f\left(\frac{\Delta a}{a_0}, \theta\right) = G_0 \cdot f\left(\frac{\Delta a}{a_0}, \theta\right), \tag{29}
$$

where G_0 is the energy release rate for a horizontal opening, and f is a dimensionless function describing the effect of the finite crack length (Δa) and its direction (θ):

$$
f\left(\frac{\Delta a}{a_0}, \theta\right) = \alpha\left(\theta\right)\left(\frac{\Delta a}{a_0}\right)^2 + \beta\left(\theta\right)\frac{\Delta a}{a_0} + \gamma\left(\theta\right). \tag{30}
$$

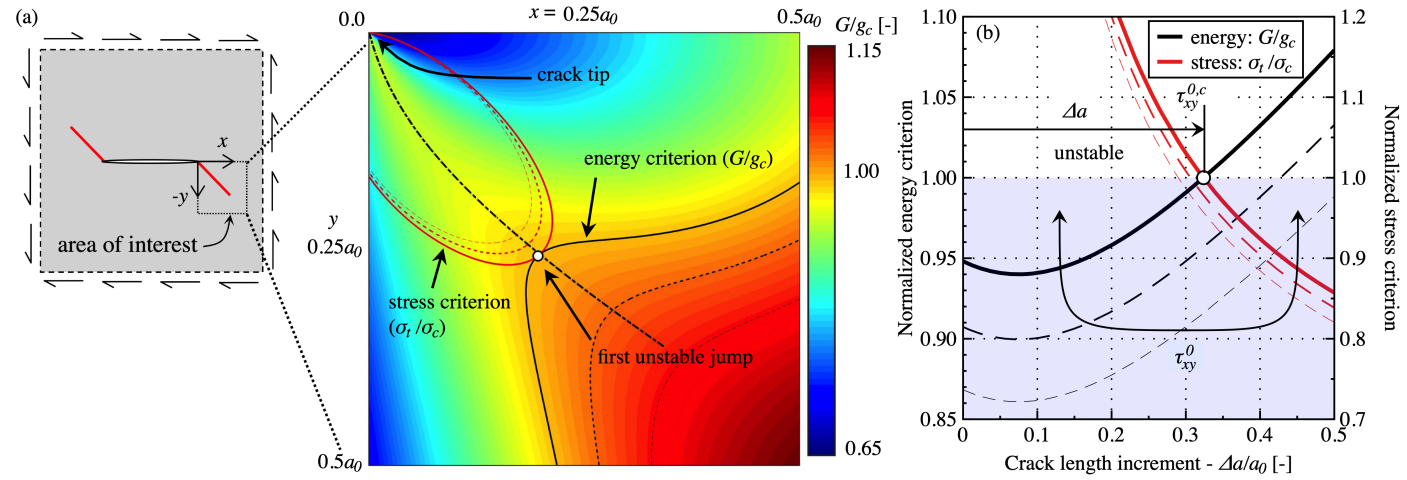

Figure 9: Coupled stress and energy criteria in the case of shear (mode II) fracture with low tensile strength (unstable initiation). (a) The colored plot shows the normalized energy criterion. With black the isocurve is shown where $G/g_c = 1$. While with red curves the stress criterion is highlighted as a function of the increasing load ($\sigma_t/\sigma_c = 1$). Hollow circles show the position and the initiation length where both criteria are just satisfied, and the crack can propagate. (b) Both normalized criteria are shown on the path of the local maximum energy release rate as a function of the distance from the crack tip. Hollow circle shows the distance of the first unstable jump.

From the analytic solution we know that $\alpha(0) = 0$, $\beta(0) = 1$ and $\gamma(0) = 1$. Additionally, the values of $\gamma(\theta)$ are available without a closed-form expression from the solution of Wu (1978).

Based on the finite element calculation, the form of functions $\alpha(\theta)$, $\beta(\theta)$ and $\gamma(\theta)$ are given based on a semi-empirical fit:

$$\alpha(\theta) = -\alpha_{\max}\sqrt{\tanh\left(\left[(\theta + 90°)\,\frac{\alpha_s}{\alpha_{\max}}\right]^2\right)} + \alpha_{\max}, \tag{31}$$

$$\beta(\theta) = 2\sqrt{\tanh\left(\left[(\theta + 90°)\,\frac{\beta_s}{2}\right]^2\right)} + 1, \tag{32}$$

$$\gamma(\theta) = \frac{\gamma_{\max} + 1}{2} - \frac{\gamma_{\max} - 1}{2}\cos\left(\theta \cdot \frac{180°}{\theta_{\max}}\right). \tag{33}$$

Parameters $\alpha_{\max}$, α_s, and β_s were set according to the finite element calculations, while $\gamma_{\max}$ (maximum increment) and $\theta_{\max}$ (angle at maximum increment) were taken from the analytic solution of Hayashi and Nemat-Nasser (1981):

$$\begin{aligned} \alpha_{\max} &= -0.014303 \\ \alpha_s &= 0.58415 \\ \beta_s &= 0.045113 \\ \gamma_{\max} &= \gamma(\theta_{\max}) = 1.517 \\ \theta_{\max} &= -75.74° \end{aligned} \tag{34}$$

The maximum difference between the fitted function and the finite element calculation was 1.17%, the goodness of fit of $\gamma(\theta)$ to the analytic values was $R^2 = 0.99$, and the maximum difference was smaller than 1%.

The critical stress defined by the Griffith criterion for pure shear fracture is:

$$\tau_{xy}^{0,c} = \sqrt{\frac{8\mu g_c}{f_c a_0 \pi\,(\kappa + 1)}}, \tag{35}$$

where $f_c = 1.504$ corresponds to the local extremum (saddle point) of the increment function at $\Delta a/a_0 = 0.075$, as seen in Fig. 9(b) and (d).

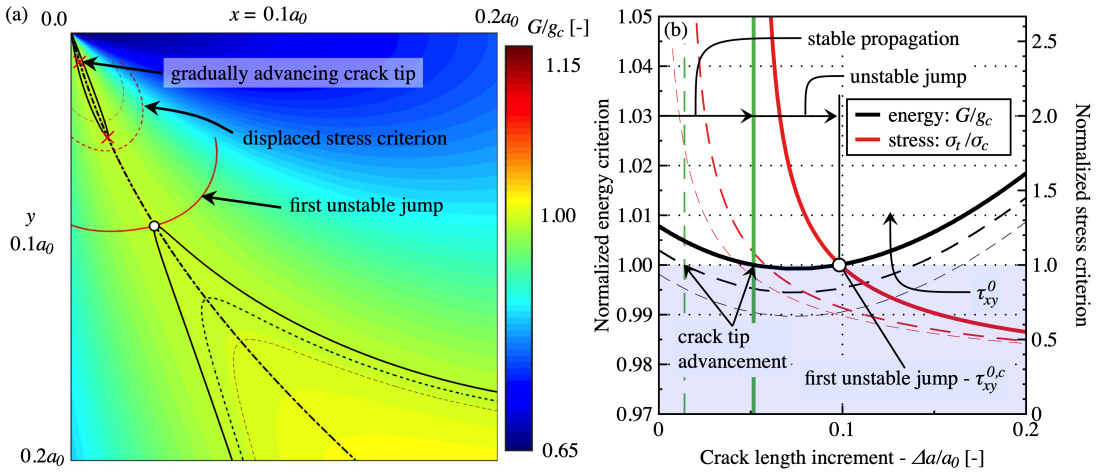

Figure 10: Coupled stress and energy criteria in the case of shear (mode II) fracture with high tensile strength (stable initiation). (a) Red curves represent the state of the stress ($\sigma_t/\sigma_c = 1$), black curves with the colored plot show the state of the energy criterion (G/g_c). (b) Similarly to Fig. 9, the two criteria are shown along the assumed propagation path. Hollow circles show the position and the initiation length where both criteria are just satisfied, and the crack can propagate. Due to the stable initiation, the original crack front advanced, and the crack tip became displaced. This phenomenon is shown with red crosses in part (a) and green lines in part (b).

For mode I, the crack path was assumed to be known, however for mode II fracture, not only the critical shear stress and the initiation length but also the propagation angle was unknown. Therefore, in contrast to Fig. 3, in the case of mode II, the spatial intersection of two curves should be determined. This is shown in Fig. 9(a) where the spatial distribution of the fracture energy ratio is depicted. The values of $G/g_c = 1$ are highlighted with black curves for different loading states. It can be seen that in this case, the criteria was not satisfied by only one point but by a whole isocurve. The isocontours of the tangential stress to strength ratio ($\sigma_t/\sigma_c = 1$) are also displayed with red lines. Similarly to the energy criterion, for a given loading state, the stress criterion was fulfilled for an infinite number of points on the curve. Initially, for a small enough imposed loading, the domains defined by the two criteria (dashed red and black lines) did not intersect: indeed, no crack increment was observed with any angles. By increasing the load, the two criteria approached each other, and when a single shared point (hollow circle) was reached, the crack started to propagate. This point determined both the initiation length and propagation angle.

Similarly to Fig. 3 we can plot the normalized criteria along the assumed initiation path: the local maximum of the energy release rate (highlighted with a dash-dot line in Fig. 9(a) and 10(a)). This is shown in Fig. 9(b) and 10(b). Similarly to the tensile fracture when the to curves intersect at $\sigma_t/\sigma_c = G/g_c = 1$, the crack will start to propagate. Interestingly we found a small decay in the maxima of G at $\Delta a/a_0 = 0.075$, which suggests a second type of behavior.

If G decreases initially, and the tensile strength is sufficiently high, it is possible that the two criteria become satisfied at the crack tip. However, as both functions decrease, the propagation is first stable as there is a part where G/g_c is not yet satisfied. The effect of this propagation is depicted in Fig. 10, which means that spatially not only one point but a surface satisfies both criteria. The coupled criterion cannot discriminate among all these configurations. Consequently, we assumed that the crack would start propagating on the local maximum of G, but displacing the crack tip and the stress singularity. This is shown in Fig. 10(a) with red circles and in Fig. 10(b) with greed dashed lines. Finally, when a common point was reached where dG/da was positive, the sample broke.

In Fig. 11(a), the critical stress is shown normalized by the Griffith solution (eq. 35) for different initial crack lengths as a function of the tensile strength. In Fig. 11(b), on the other hand, the initiation angle is depicted as a function of σ_c. The solid symbols show the initially stable propagation and the hollow ones depict the unstable first jumps. For $a = 2$ mm, we highlighted different regions: (i) the initial white part from $\theta_c \approx 75°$ is the region where the stable propagation took place, (ii) while the blue part represents the first unstable jump. If σ_c is sufficiently low, the energy criterion is only satisfied only at distances larger than the local minimum wherefore no stable initiation was observed.

Additionally, it is interesting to see that the crack initiated not only in a single direction, but could choose its propagation according to the material and the geometry. This observation was in agreement with the experimental results of Richard et al. (2014).

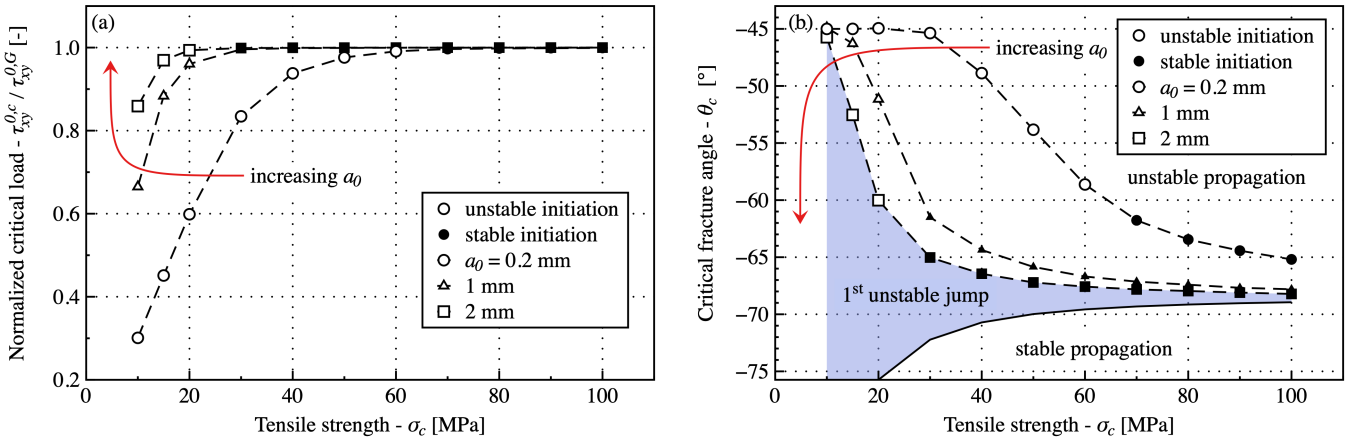

Figure 11: (a) Critical load normalized by the Griffith criterion (see eq. 35) as a function of tensile strength. (b) The angle at which the unstable crack propagation starts as a function of tensile strength. The solid symbols show cases where the crack initiation is stable; hollow symbols represent unstable ones. In the stable cases, the initiation followed the local maximum path of G until the first unstable jump.

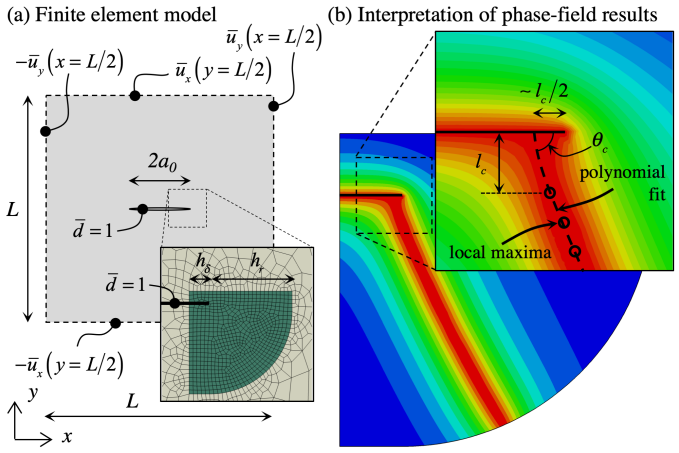

Figure 12: (a) Finite element model for mode II shear fracture. (b) Interpretation of the phase-field results and the calculation of the critical initiation angle (θ_c).

Phase-field. To test the hypothesis established using the coupled criterion, the model shown in Fig. 12 was developed using the phase-field approximation.

L was taken with a similar value as in the previous case: $L = 250a_0$. The nodes on the crack lip were doubled to include an infinitesimally small slit with a prescribed Dirichlet boundary condition in the phase-field set to 1. An observation region around the crack tip was formed with a radius of $h_r = 10l_c$ (see Fig. 12(a) green region), where the finite elements were refined according to $l_c/h = 10$. The simulation was run until the crack reached the boundary of the observation region. To apply the loading, the sides of the sample were displaced according to Fig. 12(a). The material properties were set according to Tab. 1.

When the crack was diffused, it became challenging to measure its exact path. Therefore, to extract the initiation angle, the local maxima of the damage field was identified from a distance larger than l_c, as shown in Fig. 12(b)with small circles. Subsequently, these positions were fitted with a third-order polynomial, which was then extrapolated to the crack lips.

This section deals with the crack topology and not the critical stress, as the loading case with $a_0 = 0$ was equivalent to the geometry presented in the first section, only with a different σ_2/σ_1 ratio. Therefore, only the limit cases are compared in Tab. 2. It is shown that for a small crack, the homogeneous solutions were in good correspondence with the critical values obtained with the phase-field model. In the case of a large a_0, the results were much closer to the solution of

Initial crack length (a_0) [mm]	Griffith's solution ($\tau_{xy}^{0,G}$) [MPa]	Phase-field [MPa]	Homogeneous solution [MPa]
10^{-3}	469.77	17.86	18.00
10	4.69	4.99	

Table 2: Critical shear stress ($\tau_{xy}^{0,c}$) calculated with different approaches and two initial crack lengths (a_0) with $l_c = 0.35$ mm.

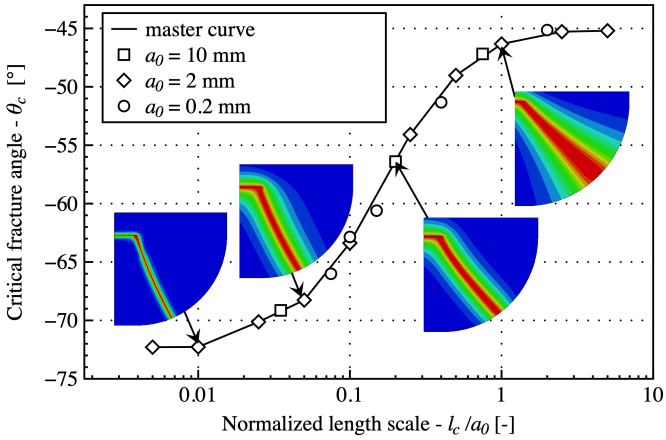

Figure 13: Critical fracture angle (θ_c) as a function of the length scale parameter (l_c) for different models.

Griffith (eq. 35).

Compared with the tensile strength, the advantage of the length scale parameters is that it introduces an internal size. Therefore, Fig. 13 shows the initiation angle as a function of a dimensionless regularization length, l_c/a_0, which indicates that the propagation and initiation depend only on the ratio of the original crack length and l_c, this is in good correspondence with the results of the energy landscape defined for the coupled criterion, as the local minimum is found at $0.075a$. As can be seen in Fig. 13, the initial crack length had no effect on the results, thus a master curve could be defined.

With small l_c the crack initiates at an angle around $\sim -73°$, which is in good correspondence with the values obtained using the coupled criterion ($\theta_c \in [-75°, -69°]$). The only difference is that due to the regularization, the stable-unstable transition is very hard to identify. In the phase-field simulations, we almost always observed a small initial stable region where the reaction force continues to increase. On the other hand, with a large l_c value, the crack inclination is $-45°$, which is in agreement with both a theoretical and coupled criterion point of view.

As shown in Fig.11(b), for a given initial crack length, the inclination angle is sensitive only to a range of chosen σ_c values. Therefore, to establish the correlation between l_c and σ_c based on the initiation angle, a_0 was varied. First, a range of a_0 was determined for a given σ_c, where the initiation angle lay between -61° and -46°. Then we subdivided the obtained a_0 interval and calculated θ_c. Each initiation angle was then interpolated between the phase-field results to obtain a normalized length scale. Finally, the value was multiplied with the initial crack length to determine l_c as a function of σ_c and θ_c.

Fig. 14 shows the correlation between l_c and σ_c. The blue area depicts the variation induced by the chosen θ_c value. It is visible that there was a small variation, but results quickly converged from -55°. Using higher inclination angles may introduce a numerical error due to the difficulty in the angle measurement in phase-field calculations. The topological correlation is in agreement with the homogeneous solution (established based on critical stress).

To test if finite-size has an effect on the initiation angle the specimen proposed by Ayatollahi and Aliha (2009) was tested, as shown in Fig. 8(b). We used $l_c = 0.3$ mm. The initial crack length was 22.5 mm, thus $l_c/a_0 = 0.0133$, which indicated a Griffith-like brittle response according to Fig. 13. Therefore, no further impact was expected from the additional reduction of l_c. The thickness of the plate was assumed to be 5 mm.

Fig. 15 shows both qualitative and quantitative comparisons between the experimental measurement (Ayatollahi and Aliha, 2009) and the phase-field simulation.

The initiation angle in the simulation (77.8°) corresponded well to the experimental measurements (78°). While the

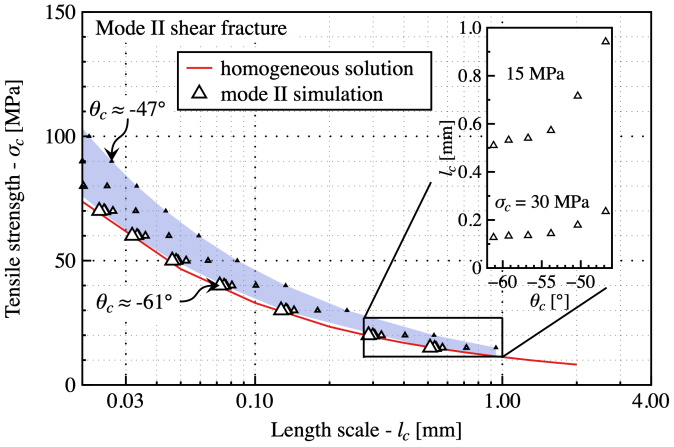

Figure 14: Critical tensile strength (σ_c) as a function of of l_c with different critical fracture angles (θ_c) for mode II shear fracture. The inset shows the convergence of l_c as a function of θ_c.

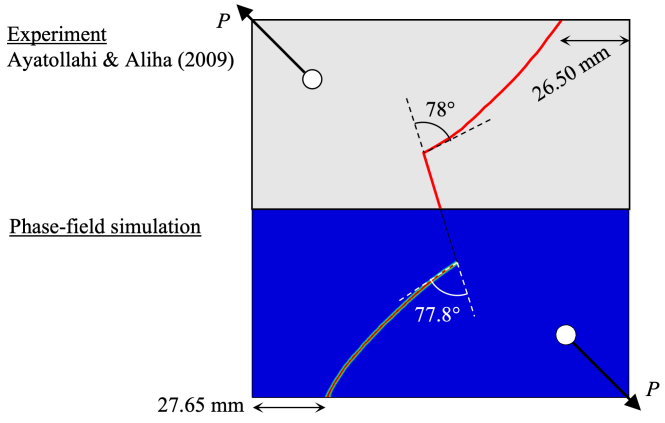

Figure 15: Phase-field results compared to experiments for the diagonally loaded square plate specimen.

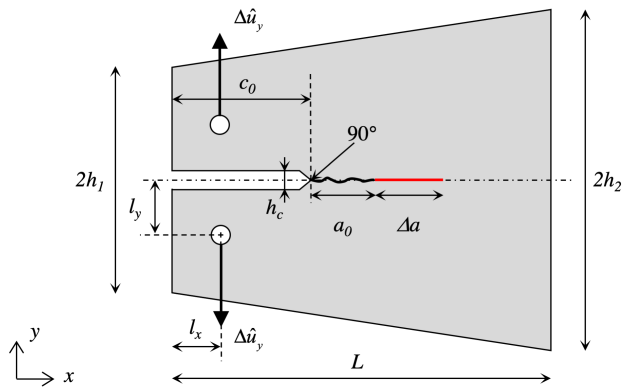

Figure 16: Tapered double cantilever beam (TDCB) geometry: $L = 100$ mm, $h_1 = 45$ mm, $h_2 = 30$ mm, $l_x = 12.8$ mm, $l_y = 14$ mm, $c_0 = 36.5$ mm, $h_c = 5$ mm. Due to symmetry, only the upper part was modeled.

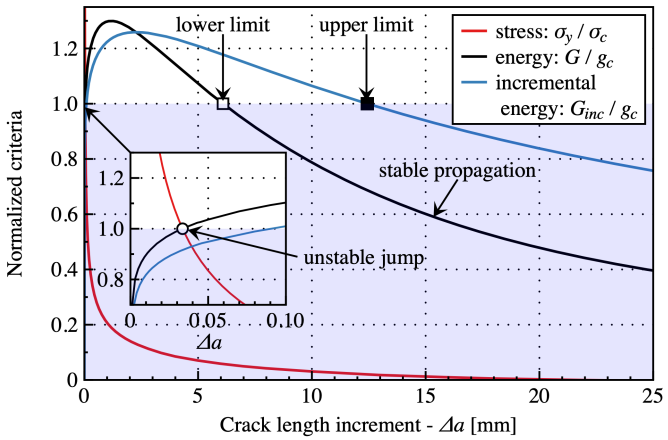

Figure 17: Coupled stress and energy criteria for the TDCB specimen.

distance between the arrival of the crack and the corner of the specimen differed only by 1.15 mm.

In conclusion, the topological correlation was in correlation with the homogeneous solution for the *standard* solution, while the *elastic threshold* introduced a higher resistance but left the crack topology relatively unchanged.

3.3. Stable propagation in the TDCB specimen

The final comparison is focused on the tapered double cantilever beam (TDCB) (Grabois et al., 2018). This geometry is particular due to the crack initiating in an unstable way, but after a well-defined distance, it stops. This section aims to test whether the phase-field method can follow an unstable-stable transition, and if the arrest length can give an additional correlation between l_c and σ_c.

Coupled criterion. The geometry of the TDCB sample is depicted in Fig. 16. As can be seen, the initial crack length varies, and in the case of the TDCB geometry, neither the tensile stress nor the energy release rate is available analytically. For this reason, the finite element method was used to determine the two functions. For the coupled criterion the stress function was calculated using a mesh densified around the crack tip. The smallest element size was chosen to be 0.5 μm. The energy release rate was calculated similarly to the shear problem: a seam crack was defined, and the opposite nodes were gradually separated. Finally, the derivative of the global potential energy was taken in respect to the crack length, using the finite difference method as shown in eq. (12) and (13). Essential to note, that to obtain smooth results, the energy difference has to be calculated on the same mesh. The material properties were set according to Tab. 1.

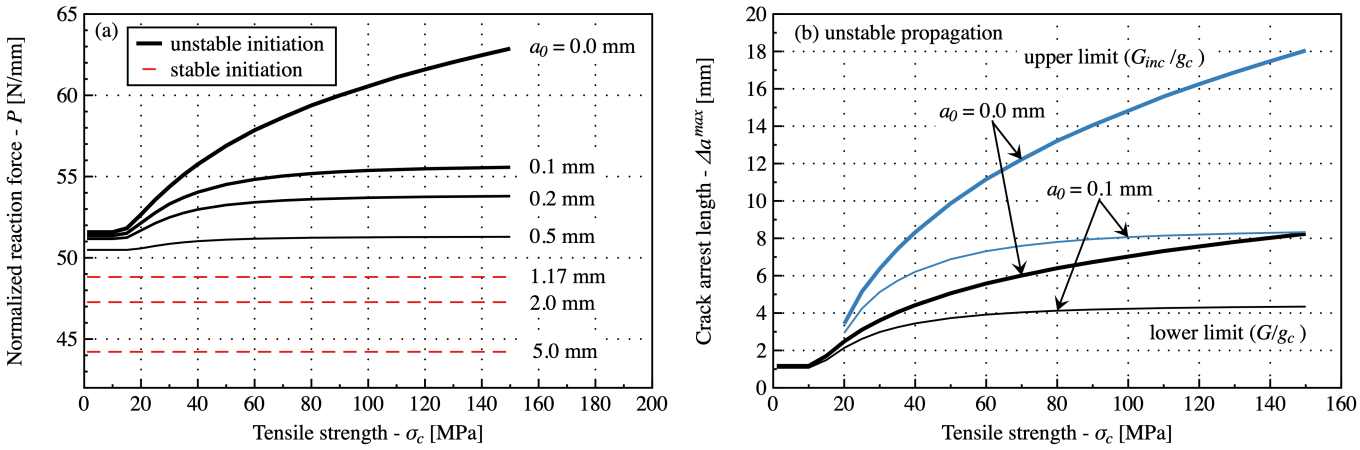

Figure 18: (a) Normalized reaction force at initiation as a function of tensile strength (σ_c) and initial crack length (a_0). (b) Crack arrest length for $a_0 = 0.0$ mm and 0.1 mm initial crack length.

The normalized criteria are presented in Fig. 17. The inset illustrates the smallest length where both stress and energy criteria are satisfied (hollow circle), while the global figure shows the evolution of the energy release rate as a function of the crack length.

The crack propagated as long as the energy criterion was fulfilled. Therefore, we plotted both instantaneous and incremental G, which defined a lower (hollow square) and an upper limit (solid square) for the arrest length. The energy release rate was not monotonous. In the case of $a_0 = 0$, the energy release rate at $\Delta a = 0$ was zero, since the Griffith criterion cannot be used if there is no sharp crack at the beginning. After this, G first increased according to a power law. At $\Delta a = 1.17$ mm, we found a global maximum, after which the function decreased monotonously. For $\Delta a = L$, G became zero as there was no longer any stored energy in the sample. After the first unstable jump, the energy release rate decreased monotonously wherefore the propagation became stable.

Fig. 18(a) shows the critical reaction force where the first crack initiated. It can be seen that if $a_0 = 0$, the result diverged as a function of σ_c. Due to the fact that $\lim_{a \to 0} G(a) = 0$, there was no critical solution for the energy criterion by itself. Therefore, the theoretical resistance went to infinity. As a result, when no sharp crack is present, it is crucial to use the coupled criterion. However, when a small initial crack was present, G started from a finite value, and quick convergence was thus shown as a function of σ_c. In the third stage, when $a_0 \geq 1.17$ mm, the initiation became stable, and the resistance depended only on the Griffith criterion, while the first initial plateau up to $\sigma_c = 15$ MPa indicated that the stress criterion was satisfied beyond the local maximum.

Similarly to the reaction force, without an initial crack, the predicted arrest lengths shown in Fig. 18(b) diverged as a function of σ_c, whereas they became convergent with small a_0. The upper limit of the arrest length could not be interpreted in case of low strength values as the crack started to propagate before than $G_{inc}/g_c \geq 1$ was satisfied.

Phase-field. The corresponding phase-field model was developed similarly to the previous examples. The initial crack was defined using the Dirichlet boundary condition in the damage field. When $a_0 = 0$, the phase-field value on only one node was predefined. The loading was applied to the hole using a rotating pin to avoid nonphysical constraints. To determine the crack length, the fracture surface energy was normalized by g_c and the thickness: $\Delta a = \frac{W}{g_c w}$.

The comparison between l_c and σ_c was made based on three quantities: (i) reaction force, (ii) arrest length based on G and (iii) G_{inc}. The obtained results are shown in Fig. 19. It can be seen that the correlation established using the instantaneous energy release rate and the reaction force were close to each other as well as to the mode I homogeneous solution. Therefore, the incremental energy release rate underestimated the tensile strength. Consequently, its use should be limited for this comparison. These results reinforce that the finite element phase-field calculation recalculated the energy state of the system step by step and reordered the elastic stresses during the propagation. Even if the unstable initiation can be considered very fast, it was not instantaneous, not even when using a quasi-static approach.

In Fig. 19, the result obtained using the phase-field simulation is plotted. While, Tab. 3 contains critical loading values with $a_0 = 0$ and $a_0 = 5$ mm. The instances with $a_0 = 0$ show that, similarly to the coupled criterion, the results

Length-scale (l_c) [mm]	Maximum reaction force - P^{max} [N/mm]	
	$a_0 = 0$	$a_0 = 5$ mm
0.05	59.41	no data
0.1	57.45	46.39
0.2	55.48	45.96
0.3	54.28	45.53
0.5	52.74	45.03
1.0	50.47	43.87

Table 3: Maximum reaction force for the phase-field simulation at fracture as a function of l_c and the chosen model.

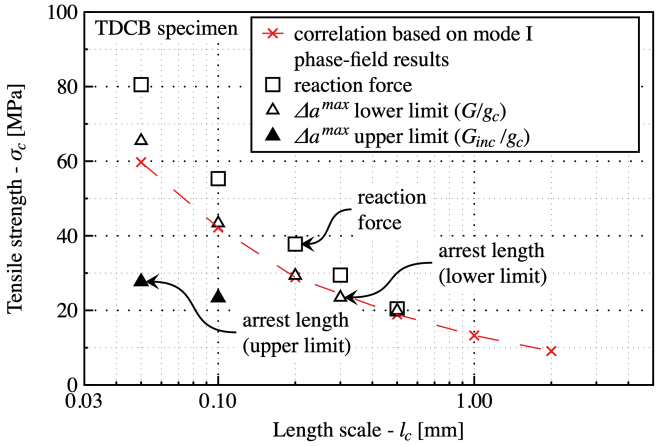

Figure 19: Correlation between the tensile strength (σ_c) and the internal length scale l_c for the TDCB specimen.

diverged. These results were slightly different from that obtained for the simple tension case shown in Fig. 4(c). However, the convergence became better if an initial crack was prescribed, but the results still depended on l_c, which is in conflict with the outcomes when using the coupled criterion and are analyzed in section 4

4. Discussion

This section is dedicated to exploring the differences between the coupled criterion and the phase-field simulations. In certain instances as shown in Fig. 6 and 19 the critical reaction force values did not exactly match the transition described using one or the other description. The major difference probably came from the fact, that while the coupled criterion assumed a singular stress field, the phase-field model was regularized. This dissimilarity could also cause deviations in the potential energy.

Generally, the correlation was clear: With a lower l_c, the strength (σ_c) increased. The correlation, however, could not be described by a single master curve. Based on the failure envelope shown in Fig. 1(b) it could vary in the range shown in Fig. 20.

In phase-field simulations, l_c is the width of the exponential function, which is the solution for the crack topology problem described by eq. (6) (Miehe et al., 2010a; Molnár and Gravouil, 2017): from the crack tip, where $d = 1$, the damage field reduces exponentially to zero at infinity. Therefore, the actual distance where the material is damaged cannot be explicitly determined, l_c provides only an estimate of the area where the material is significantly damaged. This obstacle could be tackled by changing the phase-field representation to the description of Bourdin et al. (2014), where damage is already zero at $2l_c$.

Distance, as a material parameter, does not appear explicitly in the coupled criterion either. However, the abrupt initiation length is essential to determine where both criteria are satisfied at the same time, as shown in Section 3.1. We can then substitute the critical loading back into eq. (23) to calculate the initiation length, thus the assumed process zone size. This value, as was shown in Fig. 6(b) varies with the geometry. Therefore, only the tendencies will be analyzed here. To calculate Δa_c for each l_c value the following procedure was used: (i) first the correlation between l_c and σ_c was

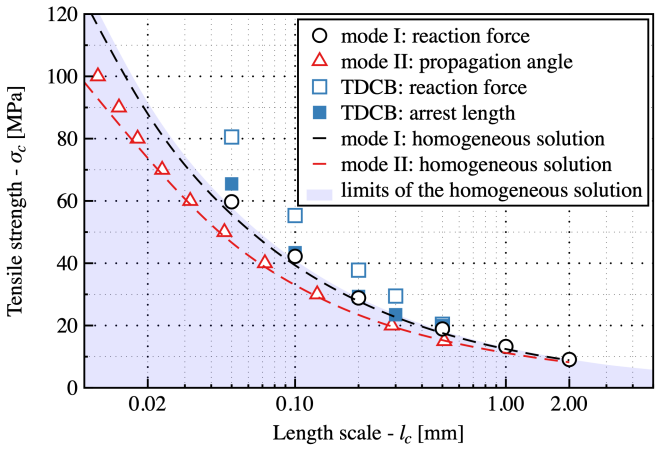

Figure 20: Summarized correlations between the tensile strength (σ_c) and the internal length scale (l_c).

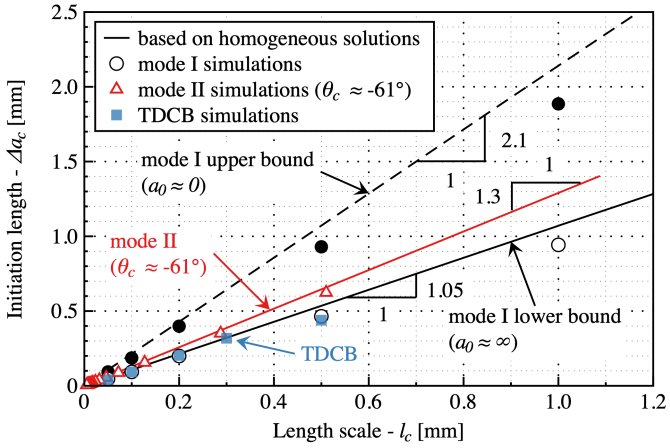

Figure 21: Summarized correlations between the initiation length (Δa_c) and the internal length scale (l_c).

established as shown in Fig. 20; (ii) then we used the identified σ_c in the coupled criterion to calculate Δa_c. For example Fig. 6(b) shows Δa_c for $\sigma_c = 29.1$ MPa ($l_c = 0.2$ mm) as a function of the initial crack length. It can be seen that the values vary between 0.2 mm (for large cracks) and 0.4 mm (for small initial defects). If we generalize this relationship the correlation between l_c and Δa_c can be plotted in Fig. 21. Black solid and dashed lines show the correlation between the two quantities for the tensile opening mode based on the homogeneous solution, while the hollow and solid circles represent the actual phase-field simulations.

Similarly to mode I, both shear (mode II) and TDCB results can be obtained with red triangles and blue squares, respectively. Stunningly all correlations are perfectly linear ($R^2 = 1.0$). Although the geometry itself affects the quantitative values, we assume that the actual initiation length (thus, the assumed process zone size and shape) is geometry dependent. This signifies that l_c can be considered an intermediate quantity between Irwin's intrinsic length and the size of the actual PZ. l_c already takes into account the local stress state, but cannot account for the macroscopic geometry. The correlation shown in Fig. 22 demonstrates that if the initiation length could be measured, it might be possible to deduce l_c and l_{mat}.

The energy release rate and the local stress maxima were determined for the phase-field model upon propagation to obtain more local details. However, calculating the energy release rate without an elastic threshold can be difficult as the crack advancement and the crack surface are not interchangeable. Due to the intrinsic nature of the damage models, a small amount of damage appears in most of them. Therefore, the global fracture surface is always going to be larger than

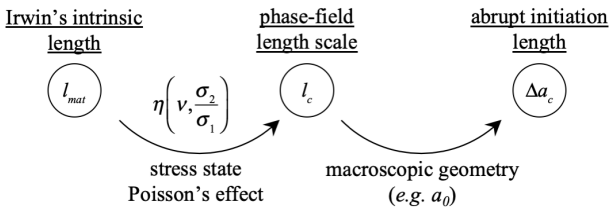

Figure 22: Correlation between the materials intrinsic length, the phase-field length scale and the initiation distance identified using the coupled criterion.

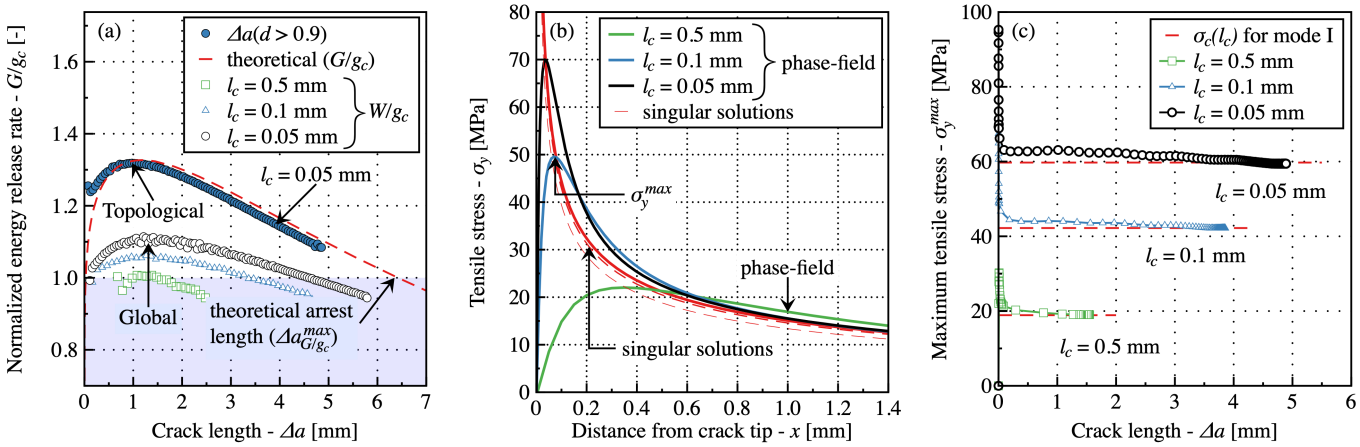

Figure 23: (a) The normalized energy release rate as a function of crack advancement. With red dashed lines, G is plotted from the coupled criterion, assuming identical reaction forces at fracture as the phase-field calculation. The hollow symbols represent phase-field results based on the global fracture surface; whereas filled symbols show the frack front position, where $d > 0.9$. (b) Tensile stress for different regularization length compared to the singular solutions for the same reaction force. (c) Maximum tensile stress (σ_y^{max}) close to the crack tip along the horizontal axis as a function of the topological crack advancement. σ_c is shown with red dashed lines for different l_c values based on Fig. 7.

the localized extent of the crack. However, it is difficult to measure the crack length based on the topology. As a consensus, a threshold of $d = 0.9$ is used. Employing the fracture topology to define crack advancement is especially difficult at the initiation stage, as energy can be lost without a topological change, since the phase-field value can increase without its propagation. The difference between topological and global crack length vanishes as l_c tends to 0. This description could be improved with the fracture surface proposed by Bourdin et al. (2014), however the implementation of such approach is difficult in a commercial finite element code like Abaqus.

Fig. 23(a) shows the energy release rate calculated for the TDCB sample with different l_c values using both global and topological approaches. It can be seen that the global approach gave a much lower value than the theoretical curve. The global criterion better described the initiation, however, it ran 5% below g_c at the arrest stage. Independently of l_c, at initiation, all simulations satisfied the energy release rate criterion. This was expected as the simulations are based on the energy equilibrium of the regularized elastic fields. The topological description is much closer to the theoretical energy release rate; however, it overestimates the initiation but remains higher when the crack stops. Presumably, the physics is better described by a mix of the two.

The discrepancy between theory and phase-fields can be explained by the difference in the stress regularization at the crack tip, as shown in Fig. 23(b). For the coupled criterion, we assumed a singular stress solution, while in the phase-field method, the stress was damaged. That is the reason why simulations with a lower l_c gradually converged to the theoretical curve.

To understand why the crack arrested before reaching its theoretical limit, in Fig. 23(c), we plotted the maximum tensile stress (σ_y^{max}) taken from the horizontal axis during the loading period until the crack arrested. It can be seen that before the initiation, the stress was much higher than the assumed limit. However, the crack started to propagate when the global energy release rate became 1.0. The crack did not start to propagate until both criteria were unsatisfied and

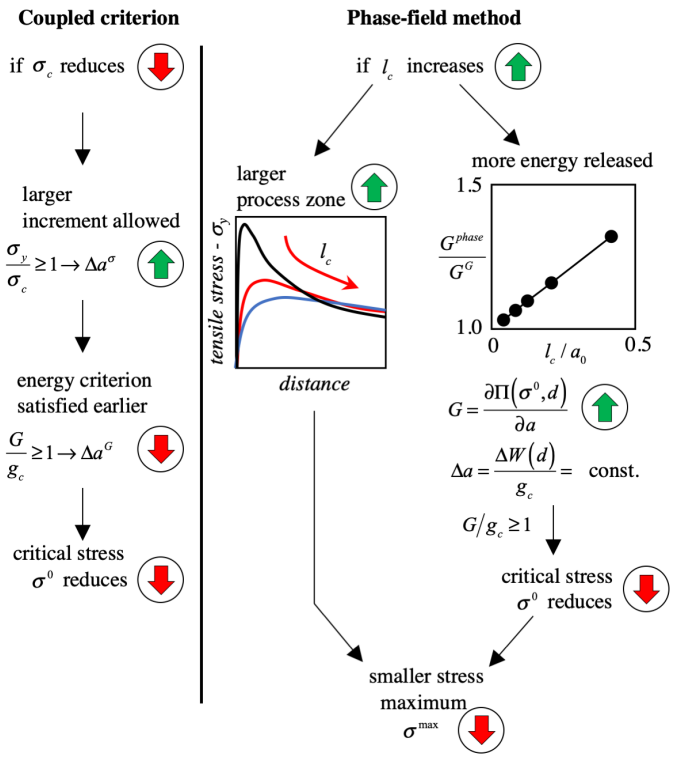

Figure 24: Schematic illustration of the workflow of the coupled criterion and the phase-field approach.

only propagated to the point when the two criteria were still satisfied. It seemed that when the stress criterion was no longer satisfied, the propagation came to a halt. The limit stress - as long as the crack propagated - was in agreement with the mode I value obtained in section 3.1. Interestingly, even if the phase-field was not based on the two criteria (stress and energy), due to the length scale parameter, it followed their principles.

The phase-field model was created to satisfy the energy-based criterion only. More precisely, if the rate of elastic strain energy released from the sample was higher than g_c, the fracture would advance. However, we showed that there existed a correlation between the maximum tensile stress and the parameter l_c. Therefore, the phase-field method itself was sensitive to a stress-based criterion, even if this correlation was indirect. This dependence is explained in Fig. 24. On the left side, the basic idea of the coupled criterion is depicted. When the tensile strength was reduced, the regularization length, thus the allowed crack increment was larger. Consequently, the Griffith criterion became satisfied earlier and a smaller applied force/stress was sufficient to induce fracture.

Using the same logic, the phase-field approach can be understood as follows. If l_c is increased, the regularization/process zone becomes larger. This causes the maximum stress to be reduced (as seen in the left inset) and also causes more damage to the elastic strain energy. A simple test was conducted: the strain energy difference was calculated between two crack lengths using predefined phase-field boundary conditions. The effect of the loading was emitted from the phase-field calculation; only the energy degradation was taken into account on a mode I tensile problem. We found that the energy released by a unit increment increased as a function of l_c. Essentially, the integrated crack surface remained constant, because the normalization in Γ included l_c, see eq. (1). In conclusion, if l_c increased the elastic energy release rate, Griffith's criterion would be satisfied earlier, causing a reduction in the critical stress/force. Thus, the combination of the smaller reaction force for a given gc and the larger regularization would result in a smaller maximum tensile stress. This correlation might be interpreted as a smaller tensile strength as a function of a higher l_c.

5. Conclusion

This article presents a comprehensive study focusing on the effect of the length scale parameter in phase-field fracture. The smeared damage approach was compared to the coupled stress- and energy-based criterion. Several elaborate

benchmark examples were shown, and results based on the critical loading, crack topology, and crack arrest length were discussed. In each case, the relationship between tensile strength and the internal length scale was established.

First, a convergence study demonstrated that the standard phase-field approach converged to Griffith's solution. Otherwise, a gradual decrease was found in the critical stress if the finite element density was increased, or the elastic strain energy increment was constrained.

Generally, we found similar quantitative and qualitative results for both the phase-field approach and the coupled criterion. In mode I tensile fracture, both methods demonstrated the experimentally observed size effect. For the mode II shear case, on the other hand, a transition in the initiation angle between 74-73° to 45° was found based on the chosen strength and length scale. Finally, the two methods were equally capable of describing the transformation from unstable to stable propagation, or in other words the crack arrest phenomenon.

Throughout our paper, we highlighted the difficulties faced when the theoretical description with a sharp discontinuity is compared with a smeared damage approach. For instance, we proposed viable solutions to measure the crack length and the initiation angle for quadratic phase-field variation. All macroscopic models demonstrated good correspondence with experimental measurements and the homogeneous solution of the phase-field method.

However, one of the most relevant results of the present paper is the unique correlation between the internal length scale, maximum tensile strength and the initiation length. We showed that this relationship could be described with a surface rather than a single curve as the stress state has a significant effect on the results. We showed that the instantaneous initiation length increases linearly with l_c, confirming that l_c controls explicitly the size of the first crack advancement. We theorized that l_c can be considered an intermediate quantity between Irwin's intrinsic length and the size of the actual process zone. We are convinced that the addition of the gradient term, *i.e.,* the diffuse representation, helps us capture more about the physics of fracture than the original Griffith method. We thus consider it essential to find a deeper microscopic explanation for the local regularization.

Our study demonstrated that energy- and stress-based criteria together are required to determine the resistance of a sample. The importance of this phenomenon is increasingly paramount when considering real-life examples where crack sizes are usually at the micrometer scale. Interestingly, we observed that even if the phase-field solution was formulated based on energy principles, it satisfied the stress criterion as well at the initiation. The difference between the coupled criterion and the phase-field solution was explained by the added regularization around the crack tip. The coupled criterion kept the infinite stress peak, while the phase-field regularized the singularity. Therefore, for the same global reaction force value, the stress and energy distributions were generally different, for which reason the global energy of the samples differed.

It should be noted that the correlation established here only relates the strength and the internal length scale based on one surface potential and one degradation function. To generalize the relationship, this should be extended to a variation of phase-field formulations. After laying down the foundation stones of the theory, the experimental observation of the stress regularization would be essential (Réthoré and Estevez, 2013).

Acknowledgment

This work was supported by the French Research National Agency program e-WARNINGS (ANR-19-CE42-0012-04).

References

Alessi, R., Vidoli, S., Lorenzis, L. D., 2018. A phenomenological approach to fatigue with a variational phase-field model: The one-dimensional case. Engineering fracture mechanics 190, 53–73.

Ambati, M., Gerasimov, T., De Lorenzis, L., 2015b. A review on phase-field models of brittle fracture and a new fast hybrid formulation. Computational Mechanics 55 (2), 383–405.

Ambati, M., Gerasimov, T., Lorenzis, L. D., 2015. Phase-field modeling of ductile fracture. Computational Mechanics 55 (5), 1017–1040.

Ambrosio, L., Tortorelli, V. M., 1990. Approximation of functional depending on jumps by elliptic functional via t-convergence. Communications on Pure and Applied Mathematics 43 (8), 999–1036.

Amestoy, M., Leblond, J. B., 1992. Crack paths in plane situations—II. detailed form of the expansion of the stress intensity factors. International Journal of Solids and Structures 29 (4), 465–501.

Amor, H., Marigo, J.-J., Maurini, C., 2009. Regularized formulation of the variational brittle fracture with unilateral contact: Numerical experiments. Journal of the Mechanics and Physics of Solids 57 (8), 1209 – 1229.

Ayatollahi, M. R., Aliha, M. R. M., 2009. Analysis of a new specimen for mixed mode fracture tests on brittle materials. Engineering Fracture Mechanics 76 (11), 1563–1573.

Bažant, Z. P., 1997. Scaling of quasibrittle fracture: asymptotic analysis. International Journal of Fracture 83 (1), 19.

Bažant, Z. P., 1999. Size effect on structural strength: a review. Archive of applied Mechanics 69 (9-10), 703–725.

Benallal, A., Marigo, J.-J., 2006. Bifurcation and stability issues in gradient theories with softening. Modelling and Simulation in Materials Science and Engineering 15 (1), S283.

Borden, M. J., Verhoosel, C. V., Scott, M. A., Hughes, T. J., Landis, C. M., 2012. A phase-field description of dynamic brittle fracture. Computer Methods in Applied Mechanics and Engineering 217-220, 77 – 95.

Bourdin, B., Francfort, G., Marigo, J.-J., 2000a. Numerical experiments in revisited brittle fracture. Journal of the Mechanics and Physics of Solids 48 (4), 797 – 826.

Bourdin, B., Francfort, G. A., Marigo, J.-J., 2000b. Numerical experiments in revisited brittle fracture. Journal of the Mechanics and Physics of Solids 48 (4), 797 – 826.

Bourdin, B., Marigo, J.-J., Maurini, C., Sicsic, P., 2014. Morphogenesis and propagation of complex cracks induced by thermal shocks. Phys. Rev. Lett. 112, 014301.

Broek, D., 1982. Elementary engineering fracture mechanics. Springer Science & Business Media.

Chudnovsky, A., 2014. Slow crack growth, its modeling and crack-layer approach: A review. International Journal of Engineering Science 83, 6 – 41, special Issue in Honor of Alexander Chudnovsky.

Cornetti, P., noz Reja, M. M., Saporaand, A., Carpinteri, A., 2019. Finite fracture mechanics and cohesive crack model: weight functions vs. cohesive laws. Int. J. Sol. Struct 156-157, 126–136.

Cornetti, P., Sapora, A., Carpinteri, A., 2013. Mode mixity and size effect in v-notched structures. Int. J. Sol. Struct. 50(10), 1562–1582.

Cornetti, P., Sapora, A., Carpinteri, A., 2016. Short cracks and V-notches: Finite fracture mechanics vs. cohesive crack model. Engng. Fract. Mech. 168, 2–12.

Doitrand, A., Estevez, R., Leguillon, D., 2019. Comparison between cohesive zone and coupled criterion modeling of crack initiation in rhombus hole specimens under quasi-static compression. Theor. App. Fract. Mech 99, 51–59.

Doitrand, A., Fagiano, C., Carrère, N., Chiaruttini, V., Hirsekorn., M., 2017. Damage onset modeling in woven composites based on a coupled stress and energy criterion. Engng. Fract. Mech. 169, 189–200.

Doitrand, A., Leguillon, D., 2018a. 3D application of the coupled criterion to crack initiation prediction in epoxy/aluminum specimens under four point bending. Int. J. Sol. Struct 143, 175–182.

Doitrand, A., Leguillon, D., 2018b. Comparison between 2D and 3D applications of the coupled criterion to crack initiation prediction in scarf adhesive joints. Int. J. Adh. Adh. 85, 69–76.

Doitrand, A., Leguillon, D., 2018c. Numerical modeling of the nucleation of facets ahead of a primary crack under modeI+III. Int. J. Fract. 123(1), 37–50.

Doitrand, A., Sapora, A., 2020. Nonlinear implementation of Finite Fracture Mecahnics: A case study on notched Brazilian disk samples. Int. J. Non-Linear Mech. 119, 103245.

Erdogan, F., Sih, G. C., 1963. On the crack extension in plates under plane loading and transverse shear. Journal of Basic Engineering 85, 519–525.

Fang, J., Wu, C., Rabczuk, T., Wu, C., Ma, C., Sun, G., Li, Q., 2019. Phase field fracture in elasto-plastic solids: Abaqus implementation and case studies. Theoretical and Applied Fracture Mechanics 103, 102252.

Farrell, P., Maurini, C., 2017. Linear and nonlinear solvers for variational phase-field models of brittle fracture. International Journal for Numerical Methods in Engineering 109 (5), 648–667.

Francfort, G., Marigo, J.-J., 1998. Revisiting brittle fracture as an energy minimization problem. Journal of the Mechanics and Physics of Solids 46 (8), 1319 – 1342.

Freddi, F., Royer-Carfagni, G., 2010. Regularized variational theories of fracture: A unified approach. Journal of the Mechanics and Physics of Solids 58 (8), 1154 – 1174.

Frémond, M., Nedjar, B., 1996. Damage, gradient of damage and principle of virtual power. International Journal of Solids and Structures 33 (8), 1083 – 1103.

García, I. G., Carter, B. J., Ingraffea, A. R., Mantič, V., 2016. A numerical study of transverse cracking in cross-ply laminates by 3d finite fracture mechanics. Compos. Part B 95, 475–487.

García, I. G., Mantič, V., Blázquez, A., 2018. The effect of residual thermal stresses on transverse cracking in cross-ply laminates: an application of the coupled criterion of the finite fracture mechanics. Int. J. Fract. 211, 61–74.

García, I. G., Paggi, M., Mantič, V., 2014. Fiber-size effects on the onset of fiber–matrix debonding under transverse tension: A comparison between cohesive zone and finite fracture mechanics models. Engng. Fract. Mech. 115, 96–110.

Gerasimov, T., Lorenzis, L. D., 2019. On penalization in variational phase-field models of brittle fracture. Computer Methods in Applied Mechanics and Engineering 354, 990 – 1026.

Grabois, T. M., Neggers, J., Ponson, L., Hild, F., Filho, R. D. T., 2018. On the validation of integrated dic with tapered double cantilever beam tests. Engineering Fracture Mechanics 191, 311–323.

Griffith, A., 1924. The theory of rupture. In: First Int. Cong. Appl. Mech. pp. 55–63.

Griffith, A. A., 1921. The phenomena of rupture and flow in solids. Philosophical Transactions of the Royal Society of London A: Mathematical, Physical and Engineering Sciences 221 (582-593), 163–198.

Gupta, A., Krishnan, U. M., Chowdhury, R., Chakrabarti, A., 2020. An auto-adaptive sub-stepping algorithm for phase-field modeling of brittle fracture. Theoretical and Applied Fracture Mechanics 108, 102622.

Hayashi, K., Nemat-Nasser, S., 1981. Energy-Release Rate and Crack Kinking Under Combined Loading. Journal of Applied Mechanics 48 (3), 520–524.

Henninger, C., Leguillon, D., Martin, E., 2007. Crack initiation at a v-notch-comparison between a brittle fracture criterion and the dugdale cohesive model. C. R. Mecanique 335, 388–393.

Irwin, G. R., 1958. Fracture. Springer Berlin Heidelberg, Berlin, Heidelberg, pp. 551–590.

Issa, M. A., Issa, M. A., Islam, M. S., Chudnovsky, A., 2000. Size effects in concrete fracture: Part I, experimental setup and observations. International Journal of Fracture 102 (1), 1–24.

Kimoto, H., Usami, S., Miyata, H., 1985. Flaw size dependence in fracture stress of glass and polycrystalline ceramics. Transactions of the Japan Society of Mechanical Engineers Series A 51 (471), 2482–2488.

Klinsmann, M., Rosato, D., Kamlah, M., McMeeking, R.-M., 2015. An assessment of the phase field formulation for crack growth. Computer Methods in Applied Mechanics and Engineering 294, 313–330.

Kumar, A., Bourdin, B., Francfort, G. A., Lopez-Pamies, O., 2020. Revisiting nucleation in the phase-field approach to brittle fracture. Journal of the Mechanics and Physics of Solids 142, 104027.

Kumar, A., Lopez-Pamies, O., 2020b. The phase-field approach to self-healable fracture of elastomers: A model accounting for fracture nucleation at large, with application to a class of conspicuous experiments. Theoretical and Applied Fracture Mechanics 107, 102550.

Leblond, J. B., 1989. Crack paths in plane situations—I. general form of the expansion of the stress intensity factors. International Journal of Solids and Structures 25 (11), 1311–1325.

Leguillon, D., 2002. Strength or toughness? a criterion for crack onset at a notch. Eur. J. Mech. - A/Solids 21(1), 61–72.

Leguillon, D., Martin, E., Seveček, O., Bermejo, R., 2018. What is the tensile strength of a ceramic to be used in numerical models for predicting crack initiation? Int. J. Fract. 212(1), 89–103.

Leguillon, D., Quesada, D., Putot, C., Martin, E., 2007. Size effects for crack initiation at blunt notches or cavities. Engng. Fract. Mech. 74, 2420–2436.

Leguillon, D., Yosibash, Z., 2017. Failure initiation at V-notch tips in quasi-brittle materials. Int. J. Solids Struct. 122–123, 1–13.

Li, J., Leguillon, D., Martin, E., Zhang, X.-B., 2019. Numerical implementation of the coupled criterion for damaged materials. International Journal of Solids and Structures 165, 93–103.

Liu, Y., Deng, C., Gong, B., 2020. Discussion on equivalence of the theory of critical distances and the coupled stress and energy criterion for fatigue limit prediction of notched specimens. Int. J. Fat. 131, 105236.

Lo, Y.-S., Borden, M. J., Ravi-Chandar, K., Landis, C. M., 2019. A phase-field model for fatigue crack growth. Journal of the Mechanics and Physics of Solids 132, 103684.

Lorentz, E., Andrieux, S., 2003. Analysis of non-local models through energetic formulations. International Journal of Solids and Structures 40 (12), 2905–2936.

Lorentz, E., Godard, V., 2011. Gradient damage models: Toward full-scale computations. Computer Methods in Applied Mechanics and Engineering 200 (21), 1927 – 1944.

Mantič, V., 2009. Interface crack onset at a circular cylindrical inclusion under a remote transverse tension. application of a coupled stress and energy criterion. Int. J. Sol. Struct. 46, 1287–1304.

Martin, E., Leguillon, D., Carrère, N., 2012. A coupled strength and toughness criterion for the prediction of the open hole tensile strength of a composite plate. Int. J. Sol. Struct. 49(26), 3915–3922.

Martin, E., Leguillon, D., Seveček, O., Bermejo, R., 2018. Understanding the tensile strength of ceramics in the presence of small critical flaws. Engng. Fract. Mech. 201, 167–175.

Martin, E., Vandellos, T., Leguillon, D., Carrère, N., 2016. Initiation of edge debonding: coupled criterion versus cohesive zone model. Int. J.Fract 199, 157–168.

Martínez-Pañeda, E., Golahmar, A., Niordson, C. F., 2018. A phase field formulation for hydrogen assisted cracking. Computer Methods in Applied Mechanics and Engineering 342, 742–761.

Mesgarnejad, A., Bourdin, B., Khonsari, M. M., 2015. Validation simulations for the variational approach to fracture. Computer Methods in Applied Mechanics and Engineering 290, 420–437.

Mesgarnejad, A., Imanian, A., Karma, A., 2019. Phase-field models for fatigue crack growth. Theoretical and Applied Fracture Mechanics 103, 102282.

Miehe, C., Aldakheel, F., Raina, A., 2016. Phase field modeling of ductile fracture at finite strains: A variational gradient-extended plasticity-damage theory. International Journal of Plasticity 84, 1 – 32.

Miehe, C., Hofacker, M., Welschinger, F., 2010b. A phase field model for rate-independent crack propagation: Robust algorithmic implementation based on operator splits. Computer Methods in Applied Mechanics and Engineering 199 (45–48), 2765 – 2778.

Miehe, C., Welschinger, F., Hofacker, M., 2010a. Thermodynamically consistent phase-field models of fracture: Variational principles and multi-field FE implementations. International Journal for Numerical Methods in Engineering 83 (10), 1273–1311.

Moës, N., Stolz, C., Bernard, P.-E., Chevaugeon, N., 2011. A level set based model for damage growth: The thick level set approach. International Journal for Numerical Methods in Engineering 86 (3), 358–380.

Molnár, G., Gravouil, A., 2017. 2d and 3d abaqus implementation of a robust staggered phase-field solution for modeling brittle fracture. Finite Elements in Analysis and Design 130, 27 – 38.

Molnár, G., Gravouil, A., Seghir, R., Réthoré, J., 2020. An open-source abaqus implementation of the phase-field method to study the effect of plasticity on the instantaneous fracture toughness in dynamic crack propagation, (in press).

Mumford, D., Shah, J., 1989. Optimal approximations by piecewise smooth functions and associated variational problems. Communications on pure and applied mathematics 42 (5), 577–685.

Nguyen, T.-T., Yvonnet, J., Bornert, M., Chateau, C., 2016c. Initiation and propagation of complex 3D networks of cracks in heterogeneous quasi-brittle materials: Direct comparison between in situ testing-microct experiments and phase field simulations. Journal of the Mechanics and Physics of Solids 95, 320–350.

Nguyen, T.-T., Yvonnet, J., Waldmann, D., He, Q.-C., 2019. Phase field modeling of interfacial damage in heterogeneous media with stiff and soft interphases. Engineering Fracture Mechanics 218, 106574.

Nguyen, T.-T., Yvonnet, J., Zhu, Q.-Z., Bornert, M., Chateau, C., 2016b. A phase-field method for computational modeling of interfacial damage interacting with crack propagation in realistic microstructures obtained by microtomography. Computer Methods in Applied Mechanics and Engineering 312, 567–595.

Nguyen, T.-T., Yvonnet, Y., Bornert, M., Chateau, C., Sab, K., Romani, R., Roy, R. L., 2016a. On the choice of parameters in the phase field method for simulating crack initiation with experimental validation. International Journal of Fracture 197 (2), 213–226.

Pham, K., Amor, H., Marigo, J.-J., Maurini, C., 2011. Gradient damage models and their use to approximate brittle fracture. International Journal of Damage Mechanics 20 (4), 618–652.

Pham, K., Marigo, J.-J., 2010a. Approche variationnelle de l'endommagement : I. les concepts fondamentaux. Comptes Rendus Mécanique 338 (4), 191 – 198.

Pham, K., Marigo, J.-J., 2010b. Approche variationnelle de l'endommagement : Ii. les modèles à gradient. Comptes Rendus Mécanique 338 (4), 199 – 206.

Pham, K. H., Ravi-Chandar, K., Landis, C. M., 2017. Experimental validation of a phase-field model for fracture. International Journal of Fracture 205 (1), 83–101.

Piero, G. D., 2013. A variational approach to fracture and other inelastic phenomena. Journal of Elasticity 112 (1), 3–77.

Poitou, B., Martin, E., Carrère, N., Leguillon, D., Gatt, J. M., 2007. Amorçage de fissure au voisinage des interfaces fibre/matrice : comparaison d'un critère mixte et des modèles de zone cohésive. 18$^{\text{eme}}$ Congrès Français de Mécanique.

Réthoré, J., Estevez, R., 2013. Identification of a cohesive zone model from digital images at the micron-scale. Journal of the Mechanics and Physics of Solids 61 (6), 1407–1420.

Richard, H. A., Schramm, B., Schirmeisen, N.-H., 2014. Cracks on mixed mode loading–theories, experiments, simulations. International Journal of Fatigue 62, 93–103.

Rosendahl, P. L., Staudt, Y., Schneider, A. P., Schneider, J., Becker, W., 2019. Nonlinear elastic finite fracture mechanics: modeling mixed-mode crack nucleation in structural glazing silicone sealants. Materials and Design 182, 108057.

Sapora, A., Torabi, A. R., Etesam, S., Cornetti, P., 2018. Finite fracture mechanics crack initiation from a circular hole. Fatigue & Fracture of Engineering Materials & Structures 41 (7), 1627–1636.

Sargado, J. M., Keilegavlen, E., Berre, I., Nordbotten, J. M., 2018. High-accuracy phase-field models for brittle fracture based on a new family of degradation functions. Journal of the Mechanics and Physics of Solids 111, 458–489.

Sih, G. C., 1974. Strain-energy-density factor applied to mixed mode crack problems. International Journal of fracture 10 (3), 305–321.

Singh, N., Verhoosel, C., de Borst, R., van Brummelen, E., 2016. A fracture-controlled path-following technique for phase-field modeling of brittle fracture. Finite Elements in Analysis and Design 113, 14 – 29.

Stein, N., Weißgraeber, P., Becker, W., 2015. A model for brittle failure in adhesive lap joints of arbitrary joint configuration. Composite Structures 133, 707–718.

Strobl, M., Seelig, T., 2020. Phase field modeling of hertzian indentation fracture. Journal of the Mechanics and Physics of Solids 143, 104026.

Sun, C.-T., Jin, Z.-H., 2012. The elastic stress field around a crack tip. Fracture Mechanics, 25–75.

Tanné, E., Li, T., Bourdin, B., Marigo, J.-J., Maurini, C., 2018. Crack nucleation in variational phase-field models of brittle fracture. Journal of the Mechanics and Physics of Solids 110, 80–99.

Weißgraeber, P., Leguillon, D., Becker, W., 2016. A review of finite fracture mechanics: crack initiation at singular and non-singular stress raisers. Archive Appl. Mech. 86(1-2), 375–401.

Wheeler, M., Wick, T., Wollner, W., 2014. An augmented-lagrangian method for the phase-field approach for pressurized fractures. Computer Methods in Applied Mechanics and Engineering 271, 69 – 85.

Wilson, Z. A., Landis, C. M., 2016. Phase-field modeling of hydraulic fracture. Journal of the Mechanics and Physics of Solids 96, 264–290.

Wu, C.-H., 1978. Fracture Under Combined Loads by Maximum-Energy-Release-Rate Criterion. Journal of Applied Mechanics 45 (3), 553–558.

Wu, J.-Y., 2018b. Robust numerical implementation of non-standard phase-field damage models for failure in solids. Computer Methods in Applied Mechanics and Engineering 340, 767 – 797.

Wu, J.-Y., Huang, Y., 2020. Comprehensive implementations of phase-field damage models in abaqus. Theoretical and Applied Fracture Mechanics 106, 102440.

Xia, L., Yvonnet, J., Ghabezloo, S., 2017. Phase field modeling of hydraulic fracturing with interfacial damage in highly heterogeneous fluid-saturated porous media. Engineering Fracture Mechanics 186, 158–180.

Xu, R., Leguillon., D., 2019. Dual-notch void model to explain the anisotropic strengths of 3D printed polymers. J of Engng Mat. Tech. 142(1), 1–4.

Yosibash, Z., Mittelman, B., 2016. A 3-D failure initiation criterion from a sharp v-notch edge in elastic brittle structures. Eur. J. Mech. A/Sol. 60, 70–94.

Zghal, J., Moreau, K., Moës, N., Leguillon, D., Stolz, C., 2018. Analysis of the failure at notches and cavities in quasi-brittle media using the Thick Level Set damage model and comparison with the coupled criterion. Int. J. Fract. 211, 253–280.

Zhang, H., Qiao, P., 2018. A coupled peridynamic strength and fracture criterion for openhole failure analysis of plates under tensile load. Engng. Fract. Mech. 204, 103–118.

Zhang, X., Vignes, C., Sloan, S. W., Sheng, D., 2017. Numerical evaluation of the phase-field model for brittle fracture with emphasis on the length scale. Computational Mechanics 59 (5), 737–752.

Zhou, S., Zhuang, X., Rabczuk, T., 2020. Phase field method for quasi-static hydro-fracture in porous media under stress boundary condition considering the effect of initial stress field. Theoretical and Applied Fracture Mechanics 107, 102523.

Appendix A. Homogeneous phase-field solution

The homogeneous phase-field solution is obtained by neglecting the effect of the damage gradient. Therefore, eq. (4) can be simplified, and the minimization problem can be solved without spatial discretization. Based on the principal strain state, the damage variable is obtained by substituting the elastic strain energy into eq. (7):

$$d = \frac{2\psi_0^+}{g_c/l_c + 2\psi_0^+}. \tag{A.1}$$

In section 2, the material strength is given based on the maximum tensile stress (σ_1) value obtained during the deformation. The failure envelope is then plotted in the space of principal stresses. Therefore, to assess the maximum value, a solution is needed, which provides a straight stress path in the space of the principal stresses.

The principal stresses are calculated by differentiation of eq. (2) with respect to the principal strains:

$$\hat{\boldsymbol{\sigma}} = \begin{bmatrix} \sigma_1 \\ \sigma_2 \end{bmatrix} = \frac{\partial \psi}{\partial \hat{\boldsymbol{\varepsilon}}} = \mathbf{L}\hat{\boldsymbol{\varepsilon}} = \mathbf{L} \begin{bmatrix} \varepsilon_1 \\ \varepsilon_2 \end{bmatrix}, \tag{A.2}$$

$$\mathbf{L} = \begin{bmatrix} \lambda g\left(d \cdot \alpha\right) + g\left(d \cdot \alpha_1\right) 2\mu & \lambda g\left(d \cdot \alpha\right) \\ \lambda g\left(d \cdot \alpha\right) & \lambda g\left(d \cdot \alpha\right) + g\left(d \cdot \alpha_2\right) 2\mu \end{bmatrix}, \tag{A.3}$$

where α and $\alpha_{1,2}$ represent the derivatives of the part functions:

$$\begin{aligned} \alpha_i = 0 \quad &\text{if} \quad \varepsilon_i < 0, \\ 1 \quad &\text{if} \quad \varepsilon_i \geq 0, \\ \alpha = 0 \quad &\text{if} \quad tr\left(\boldsymbol{\varepsilon}\right) < 0, \\ 1 \quad &\text{if} \quad tr\left(\boldsymbol{\varepsilon}\right) \geq 0. \end{aligned} \tag{A.4}$$

In this paper, the effect of the third principal direction is neglected.

The failure envelope, shown in Fig. 1c, is calculated for various $\eta = \sigma_2/\sigma_1$ ratios. To obtain the desired η value ϵ_1 is gradually increased while searching for a corresponding ϵ_2 value based on the following relationship, which was derived from eq. (A.3):

$$\varepsilon_2 = \varepsilon_1 \frac{2\mu\eta g\left(d \cdot \alpha_1\right) + \lambda g\left(d \cdot \alpha\right)\left(\eta - 1\right)}{2\mu\eta g\left(d \cdot \alpha_2\right) + \lambda g\left(d \cdot \alpha\right)\left(1 - \eta\right)}. \tag{A.5}$$

Even if a direct relationship can be established between principal strains, the solution is more complicated, as d depends on the exact value of each positive principal strain. Therefore, an internal iteration is used to search for the precise value by recalculating d for each predicted $\hat{\varepsilon}_2$.

Finally, the maximum stress is obtained as follows:

$$\sigma^c \doteq \sigma^{\max} = \eta\left(\nu, \frac{\sigma_2}{\sigma_1}\right) \cdot \sqrt{\frac{Eg_c}{l_c}} \tag{A.6}$$

The MATLAB algorithm, which calculates the concerning η value can be found in Supplementary Materials.